Searching for transits in the WTS with difference imaging light curves

J. Zendejas[1,2], J. Koppenhoefer[2,1], R.P. Saglia[2,1], J.L. Birkby[3], S.T. Hodgkin[4], G. Kovács[4], D.J. Pinfield[5], B. Sipőcz[5], D. Barrado[6,7], R. Bender[2,1], C. del Burgo[8], M. Cappetta[2], E.L. Martín[9], S.V. Nefs[3], A. Riffeser[1], and P. Steele[2]

[1] University Observatory Munich, Scheinerstrasse 1, 81679 München, Germanye-mail: chicho@usm.uni-muenchen.de
[2] Max Planck Institute for Extraterrestrial Physics, Giessenbachstrasse, 85748, Germany
[3] Leiden Observatory, Leiden University, Postbus 9513, 2300 RA Leiden, the Netherlands
[4] Institute of Astronomy, Cambridge University, Madingley Road, Cambridge CB3 0HA,UK
[5] University of Hertfordshire, Centre for Astrophysics Research, Science and Technology Research Institute, College Lane, AL10 9AB, Hatfield, UK
[6] Depto. Astrofísica, Centro de Astrobiología (INTA-CSIC), ESAC campus, PO Box 78, E-28691 Villanueva de la Cañada, Spain
[7] Calar Alto Observatory, Centro Astronómico Hispano Alemán, C/ Jesús Durbán Remón, E-04004 Almería, Spain
[8] Instituto Nacional de Astrofísica, Óptica y Electrónica, Luis Enrique Erro 1, Sta. Ma. Tonantzintla, Puebla, Mexico
[9] Centro de Astrobiología (CSIC-INTA), Ctra. Ajalvir km. 4, 28850 Torrejón de Ardoz, Madrid, Spain

ABSTRACT

The Wide Field Camera Transit Survey is a pioneer program aimed to search for extra-solar planets in the near-infrared. The images from the survey are processed by a data reduction pipeline, which uses aperture photometry to construct the light curves. We produce an alternative set of light curves using the difference imaging method for the most complete field in the survey and carry out a quantitative comparison between the photometric precision achieved with both methods. The results show that difference photometry light curves present an important improvement for stars with J > 16. We report an implementation on the box-fitting transit detection algorithm, which performs a trapezoid-fit to the folded light curve, providing more accurate results than the box-fit model.
We describe and optimize a set of selection criteria to search for transit candidates, including a parameter calculated by our detection algorithm, the *V*-shape parameter. The optimized selection criteria are applied to the aperture photometry and difference imaging light curves, selecting automatically the best 200 transit candidates from a sample of ~475 000 sources. We carry out a detailed analysis in the 18 best detections and classify them as transiting planet and eclipsing binary candidates. We present one planet candidate orbiting a late G-type star. No planet candidate around M-stars has been found, confirming the null detection hypothesis and upper limits on the occurrence rate of short period giant planets around M-dwarfs presented in a prior study. We extend the search for transiting planets to stars with J ≤ 18, which enabled us to set a more strict upper limit of 1.1 %. Furthermore, we present the detection of five faint extremely-short period eclipsing binaries and three M-dwarf/M-dwarf binary candidates. The detections demonstrate the benefits of using the difference imaging light curves especially when going to fainter magnitudes.

Key words. Methods:data analysis-Techniques:image processing-Planets-satellite:detection

1. Introduction

In recent years, the search for exo-planets has become an interesting and exciting field in Astronomy. About thousand exo-planets have been found since Mayor & Queloz (1995) detected the first planet orbiting its host Main Sequence star. Measuring the host star radial velocity variations represents one of the most successful techniques to detect exo-planets, nevertheless only few parameters of the planetary system can be determined with this method. This changes if we search for a planet transiting its host companion. A transit occurs when a planet blocks part of the surface from the star causing a slight and periodic variation in its brightness, which can be detected by a photometric analysis. This analysis provides information of the planet and its host star and together with radial velocity measurements, important physical parameters of the transiting planet can be deduced, such as the mass and the radius.The first planetary transit signal was reported in 2000 (Charbonneau et al., 2000; Henry et al., 2000) and since this discovery, a significant number (more than 300) of exo-planets have been detected transiting their host star.

Recently, several transit missions and surveys have been designed to find and characterize new exo-planets. The most exciting and successful projects designed to detect periodic transits are the space missions Kepler (Borucki et al., 2010) and CoRoT[1] (Aigrain et al., 2008; Barge et al., 2008). Kepler was launched on March 6, 2009 to observe more than 150 000 stars and it is expected to find a large number of Earth-size planets and Super Earths. On the other hand CoRoT was originally designed to find exo-planets with properties comparable to rocky planets in our Solar System. Nevertheless, in June 2013, it was announced the culmination of the CoROT mission, after six years of successful operation.

Earth-like planets are particularly interesting because if they revolve in the habitable zone of their host star (Kasting et al., 1993), the environment may be adequate to support liquid water on the surface of the planet, which is believed to be a key for the development of life. Cool and low-mass M-dwarf stars are the most promising candidates to find Earth-like planets and Super-Earths in the habitable zone. Due to their low effective

---

[1] Convection, Rotation and Planetary Transits

temperature (T_{eff}), the habitable zone of these stars is located closer to them, therefore the change in their brightness caused by a planet orbiting within this region is more evident. For instance, an Earth-size planet orbiting a $0.08\,M_\odot$ star produces a transit of 1 % depth (Kaltenegger & Traub, 2009), a similar effect occurs when a Jupiter radius planet blocks a Sun-like star.

Searching for transiting planets at near-infrared (NIR) wavelengths provides important advantages to detect transiting planets around M-dwarfs, since the peak of the Spectral Energy Distribution (SED) of these stars falls in this spectral range. Several projects are dedicated to study transiting planets around M-dwarf, such as APACHE (Giacobbe et al., 2012), PTF/Mdwarfs (Law et al., 2012) and TRAPPIST (Jehin et al., 2011). However, so far there are only two transit projects focused on finding exo-planets around cool and low-mass stars at NIR wavelengths, the MEarth project and the Wide Field Camera [2] (WFCAM) Transit Survey (WTS). The MEarth project (Berta et al., 2012; Irwin et al., 2009) is a transit survey that operates since 2008 with 8 independent 0.4 m robotic telescopes located at the Fred Lawrence Whipple Observatory on Mount Hopkins, Arizona, and is soon expected to include eight additional telescopes in the Southern hemisphere. The survey monitors individually ~ 2000 nearby (<33 pc) M-dwarfs in the NIR and is designed to detect exo-planets as small as $2\,R_\oplus$. On the other hand, the WTS is a pioneer project operated since 2007 with observations from the United Kingdom InfraRed Telescope (UKIRT) that stands out for its particular aims and methodology. A brief description of the WTS is summarized in Section 2.1.

Traditionally, aperture photometry (AP) has been the standard technique to produce light curves in transit surveys. In 1996, a new method to study crowded fields by optimal image subtraction was presented by Tomaney & Crotts (1996) and subsequently improved by Alard & Lupton (1998). This method (usually called "difference imaging"-DI) was initially developed to study microlensing events in crowded fields. However, since the majority of transit survey targets are crowded fields (e.g. Galactic plane), image subtraction photometry has become an important tool to search for planetary transits (Pietrukowicz et al., 2010). In the past, some authors have carried out comparisons between different photometric techniques. For instance, Montalto et al. (2007) used the data from a ten-night observing campaign from 4 different ground-based telescopes to develop a quantitative test by comparing the photometric precision of 3 different photometry algorithms: AP, PSF-fitting photometry and image subtraction photometry. They compare the photometric precision as a function of the apparent visual magnitude for all photometric techniques. Due to the several factors involved in the observations (which influence directly in the measurement), such as size of the telescope, instruments or atmospheric conditions, the quality of the light curves clearly varies depending on the location of the observations. For all cases presented in Montalto et al. (2007), the best Root Mean Square (RMS) was achieved by image subtraction photometry, in some cases a difference of up to 4 mmag is observed for bright objects. On the other hand, AP and PSF fitting photometry show significant variations of the photometric precision achieved by each telescope. This discrepancy suggests that the precision obtained by a certain photometric technique may depend on the characteristics of the survey, i.e. a particular method might produce different results depending on the observing conditions. In this work, we carry out a similar analysis by comparing the photometric precision of the WTS light curves obtained by DI and AP.

Large sets of light curves usually show systematic effects that can be associated with the atmospheric extinction, detector efficiency or simply PSF changes on the detector. The *sysrem* algorithm proposed by Tamuz et al. (2005) has been widely tested and it is commonly used in transit surveys (Pont et al., 2006; Snellen et al., 2007) to decrease the number of systematics in light curves. To reduce these effects in our sample, we apply the *sysrem* algorithm and subsequently include the results in the comparison analysis.

Due to the large number of light curves in transit surveys, an efficient detection algorithm is needed to speed up the identification of planet candidates. Shortly, after the discovery of the first planet transiting its host star, several algorithms have been developed. For instance, Defaÿ et al. (2001) presented an algorithm that uses a multi-frequency Fourier fit to model periodic astronomical time series. Kovács et al. (2002) presented a box-fitting algorithm based on least squares fit of step functions (BLS) to analyze stellar photometric time series. This algorithm has shown significantly better results than previous works and it has become a popular tool to search for exo-planets in transit surveys. Recently the Transit Planet Search (TPS) algorithm (Jenkins et al., 2010) has been developed to be part of the Kepler Science Processing Pipeline to search for transit planets, which is able to achieve super-resolution detection statistics.

False-positives and false-detections are common problems that make difficult the search for exo-planets in transit surveys. A false-detection can be caused if the light curve holds a significant number of systematic outliers, which can produce fake signals, whereas a false-positive is associated to real variability of the flux from the host star, (e.g. eclipsing binary systems or intrinsic variable stars). Although false-positives and false-detections have conceptually different origins, for practical reason, in this work both scenarios are referred as false-positives. Nowadays, large scale transit surveys require strategies to efficiently weed out false-positives in candidate samples and reduce the number of light curves inspected by visual examination. Several authors have suggested methods to reduce the number of false-positives and facilitate the selection of the best candidates. For instance, Burke et al. (2006) proposed a series of selection criteria based on a χ^2-minimization equivalent to the analytic solutions provided by BLS method. Later on, Hartman et al. (2009) presented selection criteria divided in different steps, which include the signal-to-pink noise ratio (Pont et al., 2006), the number of data points in the light curves, a magnitude limit and exclusion of sources with alias periods between 0.99 and 1.02 days or less than 0.4 days. Nevertheless, the majority of selection criteria only remove false-positives not related to real astrophysical variability. In this study we propose a selection criterion, which has the ability of excluding false-positives taking into account elements from the transit detection algorithm, as well as a new criterion named "V-shape parameter" that is designed to recognize automatically eclipsing binary systems.

The structure of this paper follows the next outline: In Section 2 we describe the WTS and summarize the image reduction pipeline. In this section we also give a description of the DI analysis and describe the procedure of the light curve extraction. A quantitative comparison between the photometric precision of light curves obtained by AP and DI techniques is presented in Section 3. The Section 4 is dedicated to present our transit detection algorithm and the V-shape parameter obtained from the implementations made on the BLS algorithm. Sections 4.1 and 4.2 present our selection criteria and the optimization

---

of the parameters used to detect planet candidates on the WTS light curves. In Sections 5 and 6 we show the candidates that pass our selection criteria and a detailed physical characterization of the candidates. We present in Section 7 other applications of the WTS DI light curves, such as the detection of ultra-short period and detached M-dwarf eclipsing binaries. Finally, we summarize our results in Section 8.

2. Data analysis & methodology

2.1. The Wide Field Camera Transit Survey

Low-mass main-sequence stars of spectral type M are the most abundant stars in the Galaxy, representing about 75% of the total stellar population (Scalo et al., 2007). In addition, M-dwarfs present certain properties that make them ideal targets to search for rocky planets (Tarter et al., 2007). Motivated by this, the WTS was initially developed to monitor and search for transiting planets for the first time in the NIR. Since the transit technique is based on relative photometry, the survey can be performed in poor weather conditions, hence WTS is conducted as a back-up project, operating when the observing condition are not suitable (seeing > 1 arcsec) for the main program of the UKIRT Infrared Deep Sky Survey (UKIDSS). The survey was originally assigned about 200 nights at the 3.8m UKIRT equipped with the WFCAM, which consists of 4 Rockwell Hawaii-II arrays with 2048×2048 pixels in each panel that cover a field of view of 0.75 square degrees with a resolution of 0.4 arcsec/pixels. The 4 detectors are distributed geometrically at the corners of a square with an auto-guider located at the center of the frame. This array is usually called *pawprint*, a complete observation sequence of the WTS consists of 8 *pawprints* (a-h) and each one is built up from a nine-point jitter pattern of 10s. An entire field is completed in about 15 min, i.e, the WTS light curves have an average cadence of four data points per hour. Since the dimension and separation of the detectors have approximately the same size (∼ 13 arcmin), a uniform target field can be achieved by observing the 8 *pawprints*. Four fields were selected seasonally to be observed (RA = 03, 07, 17 and 19h) periodically during a year, thereby the WTS guarantees a reasonable continuous observations campaign. Nevertheless, this work is only dedicated to study the RA = 19h field, which has been observed until May 2011 with about 1145 epochs and contains ∼ 475 000 sources, of which ∼ 113 000 have magnitudes J ≤ 18. All observations for the WTS are done in the J-band ($\lambda_{\text{eff}} \approx 1200$nm). For more details about the WTS we refer to Kovács et al. (2013). The image reduction procedure will be described in the next section.

2.2. Image reduction pipeline

Due to the large amount of data collected by the WTS, a pipeline to process the images automatically is required. The J-band images from the WTS are reduced by the image reduction pipeline from the Cambridge Astronomical Survey Unit[3] (CASU), which is used to process all images from the WFCAM. The image reduction pipeline is based on the work developed by Irwin (1985) and later modified and adapted to the Isaac Newton Telescope (INT) Wide Field Survey (WFS) (Irwin & Lewis, 2001) and subsequently to the Monitor project (Irwin et al., 2007). The pipeline includes the following steps: De-biasing and trimming, non-linearity correction, bad pixel replacement, flatfielding, defringing and sky subtraction. A thorough description of all the

steps can be found in Irwin & Lewis (2001). Astrometry and photometry are calibrated using bright stars in the field-of-view from the 2-Micron All-Sky Survey (2MASS) (Kleinmann et al., 1994) catalog (see Hodgkin et al. 2009). Particularly, the astrometric calibration plays an important role in the DI technique, since a precise alignment of data frames is crucial to success with this method. The astrometry is described by six coefficient linear transformations allowing for scale, rotation, shear and coordinate offset corrections. The pipeline also provides master catalog and light curves, which are constructed by the AP method, using a series of soft-edge-apertures that account for the fractional area of a pixel included in the aperture, with the addition of a simultaneous redistribution of flux from nearby stars. More detailed description of the light curves and catalog can be found in Kovács et al. (2013). In the next section we describe the DI method and the process of the light curves extraction.

2.3. Difference Imaging Analysis

In addition to the standard WTS light curves (AP) generated by the CASU pipeline, we alternatively produce a second set of light curves by using DI photometry. According to Alard & Lupton (1998), the method operates on a reference image, which is the combination of the best seeing images from the data set (∼ 20 in our case). On average the seeing range of the images used to construct the reference frames is 1.18 to 1.39 arcsec. The reference frame is convolved with a kernel to match the seeing of each single image, resulting in a convolved reference image. A difference image is obtained by subtracting the convolved reference image from each single image.

Finding the optimal kernel that matches the seeing of two frames with different PSFs represents a crucial and complex problem during the DI process. Alard & Lupton (1998) proposed a method, in which the optimal kernel is approximated using a superposition of N kernel base functions, which are constituted of 2-dimensional Gaussian functions modulated with a polynomial of order p_i. The expression for the optimal kernel is :

$$K(u,v) = \sum_{i=1}^{N} exp\left[-\frac{u^2+v^2}{2\sigma_i^2}\right]\sum_{j=0}^{p_i}\sum_{k=0}^{p_i-j} a_{ijk}u^j v^k, \quad (1)$$

where u and v are the pixel coordinates of the kernel bitmap, which has the same pixel size as the images, a_{ijk} are the coefficients from the decomposition of the kernel using basis of functions and σ_i is the variance related to the Gaussian distribution. To calculate the kernel, we use four base functions (N=4) with σ_i= 1,2,3 and 0.1, while the degrees of the associated polynomials p_i are 6,4,2 and 0, respectively. The kernel size is 11x11 pixel and we consider a 1st order background polynomial to account for background difference. All free parameters, such as the a_{ijk} coefficients and the parameters associated to the background polynomial are determined by minimization of the following expression:

$$\chi^2 = \sum_{x,y}\frac{1}{\sigma_{x,y}^2}[\{(R(x,y)\otimes K(u,v)\} + B(x,y) - S(x,y)]^2, \quad (2)$$

where $\sigma_{x,y}^2$ is the variance of a Gaussian distribution used to approximate the images Poisson statistics, S(x,y) is a single image, R(x,y) is the reference frame and B(x,y) is the polynomial surface function that accounts for background

(a)   (b)
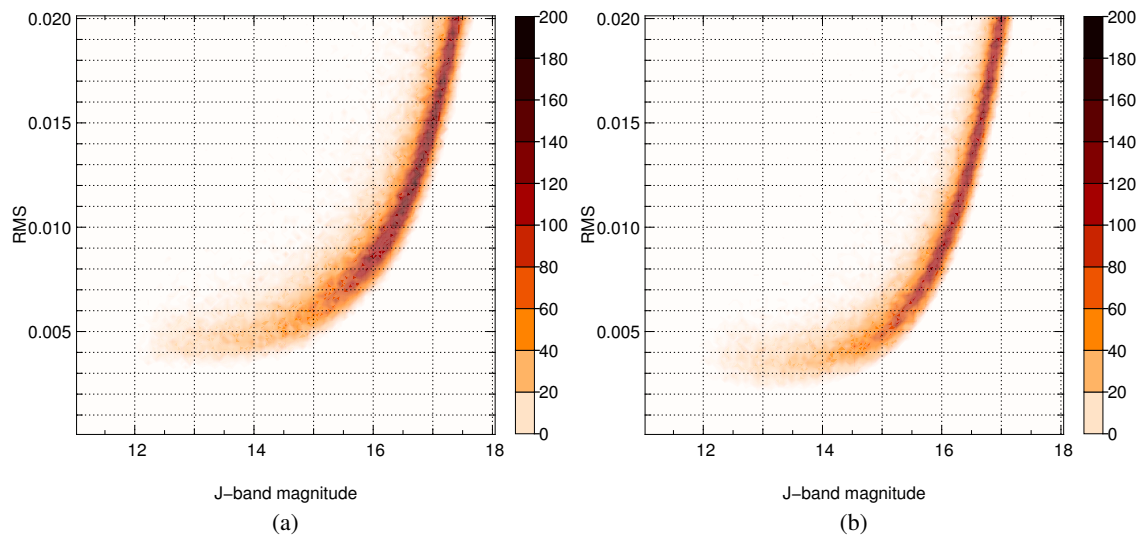
Fig. 1. Quantitative comparison between different photometric analysis. The figure shows The RMS of the DI and AP light curves (panels a and b, respectively) as a function of the J-band magnitude. The RMS corresponds to the measurements obtained after removing systematic effects. The plot is displayed in density of data points in a scale of 100 bins.

differences. Variations of PSF over the detector are a common problem in the DI technique. In order to reduce this effect during the estimation of the kernel, we divide the images in subfields and calculate the kernel in each subfield. In our case we divide the images in 10x10 subfields with a size of 200x200 pixels.

To achieve an optimized set of difference images, we tested several parameters. For each set, we extract the light curves and measure the photometric precision to verify the quality of the sample. During the testing process, we found that the light curves precision is significantly improved if we mask bright or faint stars while the difference images are produced. Two sets of difference images are created to guarantee the best quality of the light curves. In a first set, we mask all sources with magnitude ≤ 16, which provides an improvement for objects fainter than this threshold. The second set is processed by masking faint objects, i.e. all sources that hold magnitude > 16, which results in an improvement for bright stars.

2.4. Light curve extraction

From the difference images, we are able to measure the differential flux of each source. Adding the value measured in the reference image, the total flux for each single star can be estimated. Although differential fluxes are relative easy to measure in the difference images, because all constant sources are removed, estimating the fluxes in the reference frame is more difficult, especially for objects that have close neighbors. We measure the flux in the reference frame using iterative PSF-photometry. This technique is very successful to measure flux accurately in crowded fields. The method uses bright and isolated stars to extract the PSF. In a first step an initial estimation of the flux of each star is measured from the extracted PSF. In subsequent iterations, all nearby stars are removed before measuring the flux of a particular source. This process continues until all fluxes converge, using in each iteration the improved flux measured in the previous step. The fluxes measured in difference images are also estimated by PSF-photometry. The PSF is obtained from the convolved ref-

erence image, using the same stars employed to estimate the flux in the reference frame, which are a representative sample of stars in each field. Although the fluxes in the difference images certainly could be estimated by using a different photometric technique (e.g. aperture photometry), since the stellar crowd in the field is eliminated, we have chosen PSF-photometry to measure the fluxes because this method is not affected by dead pixels and does not require aperture corrections, which might lead to a wrong evaluation of the flux. Finally, the light curves are normalized to one and barycentrically time corrected using the formula of Meeus (1982). The process of extracting the light curves is applied to both sets (one optimized for bright sources and one optimized for faint sources, see previous section). We obtain the optimized set by choosing the light curve with the better photometric precision for each source.

3. Quality of the difference imaging light curves and comparison with the aperture photometry method

In this section we compare the quality of the WTS light curves produced by AP (from the CASU pipeline) and DI. A quantitative comparison between the photometric precision of both sets of light curves is performed by calculating the RMS of each single light curve from the two photometric analysis. During this process we clip all 4σ-outliers, while clipping 3 and 5σ-outliers provides similar results. Note that this step is only for the purpose of calculating the RMS and is not a final operation on the light curves.
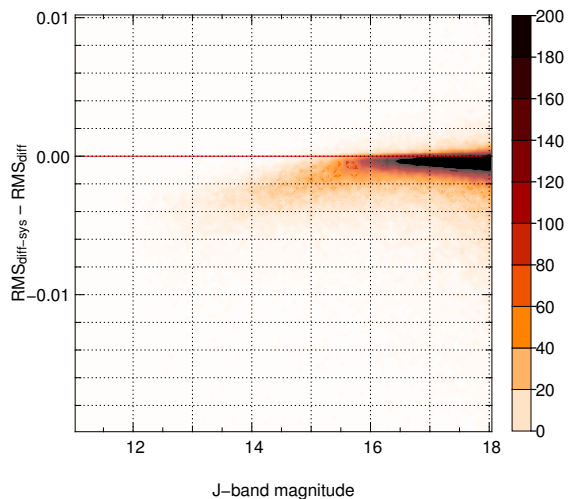
3.1. Sysrem algorithm

An algorithm to remove systematic effects in large sets of light curves from photometric surveys was proposed by Tamuz et al. (2005). The algorithm, called *sysrem*, has shown the capability of improving considerably the photometric precision of the data set by removing systematics related to the detector efficiency,

PSF variations over the detector or effects associated with the atmospheric extinction (Irwin et al., 2007; Mazeh et al., 2009). The algorithm searches for systematics that consistently appear in many sources of the sample, hence *sysrem* has the ability to remove effects without any prior knowledge of the origin of the effect.

In order to improve the quality of the light curves, we consistently apply the *sysrem* algorithm to DI and AP light curves. Note that Irwin et al. (2007) showed that the *sysrem* algorithm does not improve the precision of AP light curves by much and it might additionally produce false variability from the residuals. In our case we find a significant reduction of the scatter of constant light curves for both DI and AP light curves. Any possible false variability created by *sysrem* will not lead to the detection of false-positive candidates because of our conservative criteria applied in the candidate selection process (see below).

The results are shown in Figure 1, which represent the RMS achieved by the AP and DI light curves (panel a and b respectively) after the correction as a function of the WFCAM J-band magnitude. The DI light curves reach a precision of 3.5 mmag for bright objects in the range of $12 < J < 14$, while the RMS of AP light curves corrected by *sysrem* algorithm reaches a precision ~ 2.5 mmag in the same J-band magnitude interval. The plots show that DI produces better results for faint objects (J > 16), however in the bright magnitude range, the quality of AP light curves is slightly better. For magnitudes larger than J = 16, the DI light curves show a much higher photometric precision than the AP light curves. The RMS shows presents a difference up to 5 mmag at J = 17 mag and 15-20 mmag at J = 18 mmag.

Fig. 2. RMS difference between the DI light curves before and after applying *sysrem* algorithm. The plot shows the improvement achieved in the photometric precision once systematic effects are corrected. The plot shows the density of data points distributed in 100 bins.

These results contrast to previous studies, which compare the photometric precision achieved with both methods. For example, Montalto et al. (2007) show that DI photometry achieves an equal or better photometric precision compared to aperture and PSF photometry for all magnitudes. However, these studies were done at optical wavelengths (V-band) and a
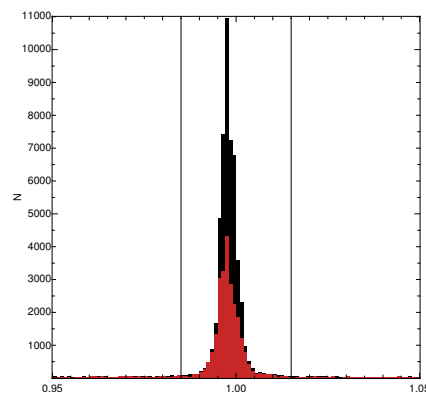

Fig. 3. Histogram of periods found by our transit detection algorithm, before (black) and after (red) applying the *sysrem* algorithm. The numbers of false detections between 0.985 and 1.015 day periods is reduced by a factor of 2.

direct comparison to a NIR survey (like the WTS) is not possible, since the detector characteristics are different. Imperfect treatment of non-linearity effects at the bright end could be one possible source for the additional systematic noise that we observe in our DI light curves. Another problem might be the non-homogeneous background, which is visible in the WTS images. We can rule out that the effect is caused by a low astrometric accuracy. Any shifts between the reference frame and the single images would produce dipole-shaped residuals in the difference image, contrary to this effect, bright sources show very symmetric noise residuals in our difference images.

In order to show the capability of the *sysrem* algorithm to improve the photometric precision, we perform a similar quantitative analysis (see above) on the DI light curves by comparing the RMS of the light curves before and after applying the *sysrem* algorithm. Figure 2 shows the RMS difference between both sets of light curve as a function of the J-band magnitude. The result of the comparative analysis indicates a significant improvement in the photometric precision of bright and faint sources when the *sysrem* algorithm is employed. A similar result is observed in the AP light curves. Note that although applying the *sysrem* algorithm results in an improvement of the photometric precision of the light curves, the capability of the algorithm to remove systematics effects is limited. Figure 3 shows the number of detected periods around the one-day alias period before and after using the *sysrem* algorithm. In an ideal case, the algorithm should account for these effects and eliminate the alias peak. In our case, the number around the alias period is reduced by a factor ~ 2 after applying the *sysrem* algorithm.

3.2. Correction of the point-by-point errors derived from the individual images

After removing systematic effects, we carried out a routine visual inspection over a random sample of light curves. We noticed that for many light curves (typically for bright sources) the scatter of the data points was much larger than the error bars. Usually error bars of light curves are estimated by a pipeline taking into in account different factors, such as the photon noise of the source, background contribution and read-out noise. However, systematic effects caused by PSF-variations or variation in noise level from the background are not included. This seems to be the case of the WTS light curves, which present a wrong esti-
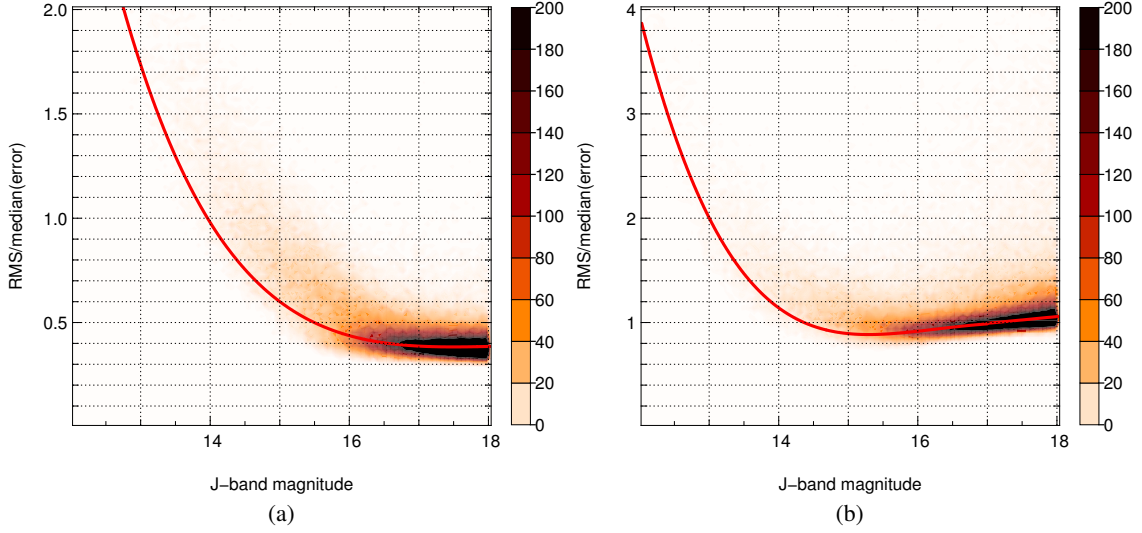
Fig. 4. Data points distribution of the RMS divided by the median error from DI and AP light curves (panel a and b respectively) as a function of J-band magnitude. The solid-red line represents the polynomial used to scale the errors bars. The plot is displayed in density of data points in a scale of 100 bins.
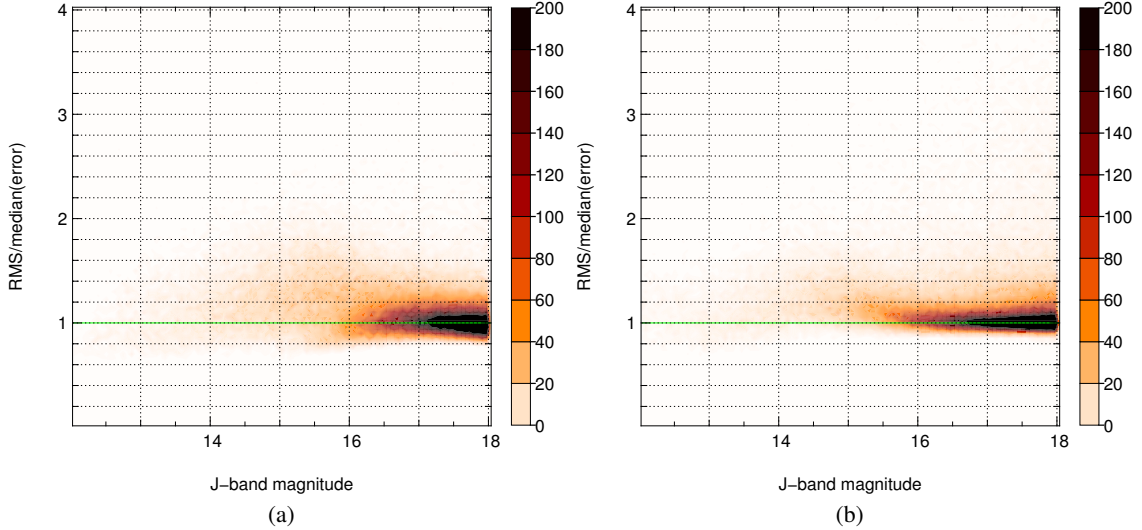
Fig. 5. Distribution of data points RMS/median(error) after re-scaling the error bars on the (a)DI and (b)AP light curves.

mation of the error bars, which is correlated to the brightness of the object. A simple way to correct the size of the error bars is to compare the RMS of the photometric measurements with the error values, since the RMS is related to the scatter level and it can be associated with the real error for non-variable objects. We perform this test for DI and AP light curves dividing the RMS by the median error calculated in each light curve. The results are shown in Figure 4, where this quotient is plotted as a function of the J-band magnitude. If the error values were correct, the RMS and median error should present similar values, therefore data points in the plots should be distributed around 1. Nevertheless, there is an evident discrepancy between both quantities, which is reflected in the shape of the data point distributions. For our work, it is important to correct the bad estimation on the error bars, since some of our selection criteria (see below) and several parameters that we estimate for our candidates later-on de-

pend on the error bars. In order to correct the error bars, we fit a polynomial (Figure 4) to the distribution of data points. The polynomial provides a scale factor as a function of the magnitude, which can be used to correct the whole sample. Note that unlike replacing the errors obtained from the images by an estimation of the scatter (RMS), scaling the error bars with a factor that is a function of the brightness of the objects, we avoid to introduce an overestimation of the errors, principally for variable sources, which can present a significant scatter in the light curves. After scaling the error bars, we perform the same test and show the results in Figure 5, where we can see that the distribution of data points clearly have been adjusted and they are now located close to 1. Nevertheless, these figures present a second higher RMS sequence for bright stars (14-16 magnitudes). We know from the AP light curves (see Kovács et al. 2013) that the WTS data present a high level of red noise (Pont et al., 2006)

also correlated to the magnitude of the objects, being the bright sources the most affected for this effect. Although the *sysrem* algorithm is designed to filter out the red noise, there is a component from the red/pink-noise that remains in the sample of light curves, which can be observed in Figure 4, where a significant scatter is visible in the distribution of the data points. The fact that *sysrem* cannot eliminate completely this component of the red/pink noise may produce fake signals and subsequently a large number of false-positives. Figure 3 demonstrates that the remaining systematics produce such effects, since a large number of objects fall into the daily alias. Nevertheless, in Section 4.1 we introduce the selection criteria used to detect planet candidate in the WTS -light curves, which have the capability to provide a pure candidate sample, ruling out false positive related to some of these systematics. On the other hand, in this work we do not use the correlated noise to measure the transit fitting significance. Therefore, the polynomial used to correct the error bars does not take into in account the dispersion of data points generated by the remaining red/pink-noise component.

4. Light curves analysis and transit detections

We detect transits in the WTS light curves using an algorithm that is based on the BLS algorithm proposed by Kovács et al. (2002). Our modifications include a trapezoidal re-fitting of the box-shaped eclipse found by BLS, where the re-fitting is done by symmetrically varying the edges of the box while keeping fixed the duration of the eclipse ("d"), which is measured at half the transit depth (see Figure 6). We emphasize that the trapezoidal shape is only fitted once the standard parameters provided by the box-fitting algorithm have been found (such as period, transit duration and epoch), however, the eclipse depth may change. We introduce the *V*-shape parameter:

$$V = \frac{2e}{f + 2e}, \tag{3}$$

where e is the duration of the ingress/egress of the eclipse in phase units and f is the duration of the transit, i.e., the flat part (see Figure 6). If e is considerably smaller than f, the *V*-shape parameter is close to 0 and the shape of the fit is box-like. On the other hand, if $f \approx 0$ and $e \gg f$, the *V*-shape parameter is close to 1 and the eclipse is "V"-shaped. One of the advantages of our modification is that the *V*-fitting results in a better estimate of the transit depth. In addition, we use the *V*-shape parameter as a selection criterion to reject grazing eclipsing binary systems which have generally very large *V* values (see next section).

We search for transit periods in the range between 0.5 and 12 days using 100 001 trial periods equally distributed in 1/P. To speed-up the calculation time, the folded light curves are re-sampled to 200 bins. The fractional transit duration was tested between 0.006 and 0.1 phase units. For each input light curve we detect the 5 best fitting periods with the BLS algorithm and then perform the trapezoidal re-fitting for each of them. We then select the period that has the lowest χ^2_{dof} of the improved *V*-fit. Figure 7 shows the difference between the reduced χ^2_{dof} of the trapezoid-fitting and the box-fitting as a function of the *V*-shape parameter. The trapezoid-fitting shows a significant improvement over the box-fitting especially for high *V* values.
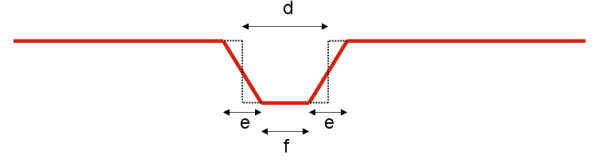

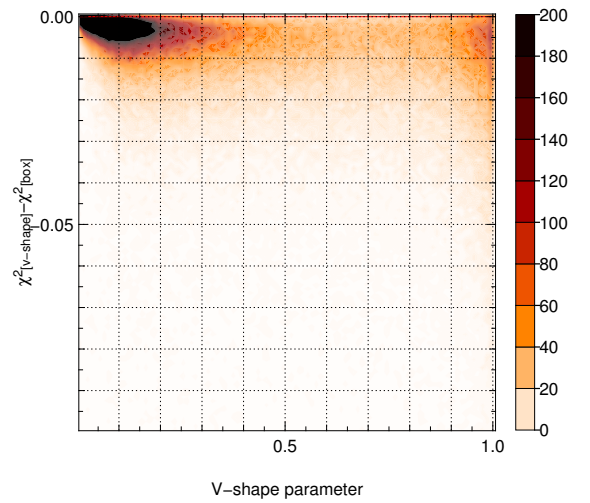**Fig. 6.** Geometry of the symmetrical trapezoid-fit.

Fig. 7. χ^2_{dof} comparison between trapezoid-fit and box-fit for transit detections. Since the box-fit is actually included in the trapezoid-fitting (i.e., *V*=0), positives values are not expected in this plot. On the other hand, a significant improvement in the trapezoid-fit is achieved specially for higher values of *V*.

4.1. Selection Criteria

Due to the large number of light curves in the WTS, it is necessary to set up a number of selection criteria to automatize the selection of candidates but efficiently reducing the number of false positives in the survey. As an initial cut we removed all objects with magnitudes J > 18. Objects below J-band = 16 are already difficult to follow-up, nevertheless we decided to extend the magnitude cut (J-band = 17) used in Kovács et al. (2013) in order to make use of the improvement achieved by difference imaging light curves for faint objects.

In addition, we reject objects for which the detection algorithm found a period close to alias periods introduced by the window function of the observing strategy. In particular we exclude objects with periods in the ranges 0.485-0.515, 0.985-1.015, 1.985-2.015 and 2.985-3.015 days. As an example, Figure 3 shows the high number of (false) detections found around the one day alias period. For the sub-field 19g1 we additionally exclude a narrow period range 1.350-1.352 days due to a very high number of false positives in this range. Based on our experience of previous works, we introduce six more selection criteria:

1. **S/N:** One of the most important criteria is the S/N of the eclipse measured from the light curves. In the past, many authors have used different ways to calculate the S/N and many different ways of utilizing it as a selection criterion. For instance Burke et al. (2006) include the signal-to-white-noise in their selection criteria to set the threshold to $S/N \geq 10$. Hartman et al. (2009) propose the same limit of $S/N \geq 10$, but in their case the threshold corresponds to the pink noise (Pont et al., 2006). Kovács et al. (2013) use the red noise to fix the detection limit, they suggest a signal-to-red noise of $S_{red} \geq 6$. Our S/N selection criterion accounts only for white noise.

2. **S/N-S/N$_{rem}$:** A large fraction of false positive detections are variable stars. To eliminate them, we use a new detection criterion, labeled $S/N - S/N_{rem}$, which is the difference of the S/N found in the BLS analysis and the S/N_{rem} found in a second pass of the algorithm after masking all points during the eclipse that has been detected in the first interaction. For a planet candidate $S/N - S/N_{rem}$ will be very high since the variability is confined to the transit phase. For variable stars, e.g. eclipsing binaries or sinusoidal variables, there is still variability left which will result in a low value of $S/N - S/N_{rem}$. Note that this criterion will eliminate the detection of systems with more than one transiting planet. However, since the WTS survey is only sensitive to periods smaller than ten days, we decided to only search for systems with a single transiting planet.

3. **# points:** Many light curves result in a high S/N detection but only very few points belong to the transit. We therefore require a minimum number of transit points in our candidate selection process. Due to the scheduling of the WTS, we do not require a minimum number of individual transits as an additional criterion, since even a small minimum number of transit points guarantees implicitly two transits or more.

4. **V$_{shape}$:** One selection criterion that has not been used in previous studies is the V-shape parameter, which was defined in the previous section. The criterion acts as a filter to eliminate false-positives generated by eclipsing binary systems. An eclipsing binary would be characterized by a very V-shaped eclipse, i.e. with a high V value.

5. **depth:** Some detections show a very deep transit signal. A typical brightness dimming corresponding to a Sun-like star and a Jupiter-like planet is about 1 %. Transit signals that are much deeper are more likely to be eclipsing binary stars. Using a cut on the maximum allowed transit depth we reduce the number of false positive detections. Note that for Jupiter-sized planets around M-dwarfs, the transit depth can be even higher than 10 %. We therefore optimize the detection criteria for M-stars independently (see below).

6. **transit duration:** In order to exclude candidates that show un-physically long eclipses we impose a limit on the fractional transit duration.

4.2. Optimization of the selection criteria

We optimize our selection criteria with Monte-Carlo simulations, where we inject transit signals in the real light curves using stellar parameter distributions (radius and mass) from the Besancon model of the galaxy (Robin et al., 2003) and the limb-darkening coefficients from Claret & Bloemen (2011). For each light curve of the WTS we pick a random star from the Besancon model that has a similar magnitude ($\Delta_{mag} \leq 0.05$) and draw a random period in the range from 0.5 to 12 days. Details about the transit injection procedure can be found in

Koppenhoefer et al. (2009).

We split the light curves in two data sets, one for F-, G- and K-stars and one for M-stars. The optimization of the selection criteria was done separately, since we expect some parameters to differ between both data sets. For instance, the transit depth is generally larger for planets orbiting M-dwarfs and the fractional transit duration is smaller. In addition, the particular analysis of the M-dwarf sample allowed us to derive an upper limit on the occurrence rate of Jupiter-sized planets around low-mass stars (see Section 6)

The M-dwarf selection is based on color cuts in seven SDSS and WFCAM bands: g-r $\geq$ 1.6, r-i $\geq$ 0.9, i-z $\geq$ 0.5, J-H $\geq$ 0.45 and H-K $\geq$ 0.17. These cuts have been derived to include the majority of M-dwarfs selected by (Kovács et al., 2013). Based on these cuts we find 10 375 M-stars brighter than 18 mag in J-band. 4 073 objects are brighter than J=17 which is slightly less but still in reasonable agreement with the number of objects selected in Kovács et al. (2013) who found 4 600 M-dwarfs using an SED fitting approach. In the following sections we report the optimized selection criteria and the detection efficiency for both data sets and present and discuss the selected candidates.

5. Candidates detected around F-, G- and K-stars

For the simulated light curves we required the detected period to be within 1% of the simulated period, allowing also a value of half or double the this period. On a computer cluster we ran in total 100 simulations. In each run we considered each light curve once for a transit injection, resulting in about 1 200 000 simulated light curves. In order to save computation time, we simulated only those cases, in which the randomly drawn inclination vector results in a visible transit signal. After running the simulations we optimized the selection criteria presented above for the DI and AP light curves of all F-, G- and K-stars. We allowed up to 100 detections on the unmodified light curves on each data set. This number is strategically selected, since it is small enough to allow a visual inspection of each detected object, while being significantly larger than the expected number of planet detections.

Tables 1 and 2 list the optimized selection criteria for the DI and AP light curves for F-, G- and K-stars and provide the number of objects that remain after applying each of the selection criteria. In this case, the fractional transit duration turned out to be a useless criterion to detect candidates around these stars. These selection criteria allow us to recover 10/26% of the signals injected into the AP/DI light curves with S/N ~ 11/18 (our minimum required S/N) and up to 80/80% with S/N $\geq$ 30/40, respectively. The resulting total efficiencies are discussed in Section 5.4. Note that before applying the magnitude limit, the number of light curves in the DI and AP data sets differ at the 10% level. This is because the object detection in the DI analysis was going slightly deeper than in the AP analysis.

In order to test whether the selection criteria differ from one to another detector we initially optimized them for each of the sub-fields independently but found almost identical values. We therefore decided to use one single set of selection criteria for F-, G- and K-stars in the the whole 19hrs field.

We visually inspected the 200 detections that pass the optimized selection criteria in the AP and DI data sets and removed candidates, which are clear eclipsing binaries with two eclipses of different depth, objects that show significant out of

Table 1. Objects removed by the selection criteria from a original sample of 464873 DI light curves.

Criterion	Remaining objects	Removed objects	%
$J \leq 18$	102428	362445	76.26
Removed alias period	72012	30416	29.69
$S/N > 18$	7080	64932	90.17
S/N-$S/N_{rem} > 8$	3391	3689	52.10
Transit points > 24	506	2285	85.08
$V_{shape} < 0.6$	288	218	43.08
Depth $\leq 4\%$	100	188	65.27
Transit duration ≤ 0.5	100	0	0.00

Notes. Number of DI candidates after applying all criteria (100).

Table 2. Objects removed by the selection criteria from a original sample of 428928 AP light curves.

Criterion	Remaining objects	Removed objects	%
$J \leq 18$	102428	326500	74.32
Removed alias period	73201	29227	28.53
$S/N > 11$	5778	67423	92.11
S/N-$S/N_{rem} > 6$	1760	4018	69.54
Transit points > 18	563	1197	68.01
$V_{shape} < 0.7$	360	203	36.06
Depth $\leq 3\%$	100	260	72.22
Transit duration ≤ 0.5	100	0	0.00

Notes. Number of AP candidates after applying all criteria selection (100).

eclipse variations and very asymmetric eclipse shapes, as well as, candidates which are too noisy to be further analyzed. We also eliminated objects that have periods below 0.5 days. Our final list of candidates includes 11 objects, of which 7 were detected in the AP-light curves and 6 are from the DI light curves. Two objects are common detections in both the DI and AP light curves, of which one candidate is WTS-2b that has recently been confirmed as a planet by the RoPACS community (Birkby et al., 2013a,b). WTS-1b is the other planet that has been found in the WTS (Cappetta et al., 2012), which was not detected by our selection criteria due to a very low S/N value.

In the following we present a detailed analysis of the 10 remaining candidates including a characterization of the host stars, a light curve fit with an analytic transit model and a test for double-eclipse binary scenarios. The analysis provides important physical parameters of the host stars and companions, which are used to asses the quality of the candidates. Figure 16 shows the folded light curves of our candidates.

5.1. Characterization of the host star

The broad band photometric measurements of the host stars of the candidates are listed in Table 3. The WFCAM provides photometry in five bands (Z,Y,J,H,K). Additional measurements in five optical bands (u,g,r,i,z) were obtained from the database of the Sloan Digital Sky Survey (SDSS 7th release, Adelman-McCarthy & et al. 2009). The table also shows in which data-set the candidate was detected (AP or DI). The candidate 19b1-02162 was found in both AP and DI data sets, in this case we use the AP light curve in the following, since it presents a lower scatter.

The characterization of the host star is essential to infer physical properties of the candidates, such as planetary radius and orbit inclination. The Virtual Observatory SED

Analyzer[4](VOSA, Bayo et al. 2008) is an on-line tool designed to automatically perform several tasks, such as the determination of stellar parameters by analyzing the SED. This analysis was carried out in our candidates using the photometry reported in Table 3. VOSA works with input parameters that can be submitted as ASCII files. They must include a reference name of the source, coordinates, visual extinction A_v, filter names, observed fluxes and the corresponding errors. Although VOSA enables us to select among 6 different fitting models, only two are appropriate for our purpose. For the F-, G- and K-stars we adopt the Kurucz ATLAS9 templates described in Castelli et al. (1997), which provide better results for a wider temperature range than the NextGen model (Baraffe et al., 1998). The program offers the option of restricting free parameters (T_{eff}, $\log g$ and [Fe/H]) to speed up the fitting process. We confine the limits to $T_{eff} = 3\,500\text{-}10\,000$K, [Fe/H]=0.0 and $\log g = 3.5\text{-}5.0$. Note that the selected values of T_{eff} and $\log g$ are compatible with main-sequence stars with spectral types between A and M. The program compares the broad band photometric measurements to theoretical synthetic spectra to find the best SED-fitting. VOSA tests a large range of stellar models within the given parameter limits. The SED-fit is also sensitive to the extinction A_v, which is used as an additional free parameter. The extinction and the corresponding SED model are obtained by testing 100 different A_v values distributed in a range from 0.01 to 1 magnitudes and selecting the value that results in the lowest χ^2 within the valid extinction range from 0.01 up to the maximum allowed extinction that is set by the total extragalactic extinction as obtained from the Galactic Extinction Calculator of the NASA/IPAC Extragalactic Database[5] (see Figure 8). In some cases the absolute minimum corresponds to an absorption that is outside the allowed range, i.e. higher than the extragalactic value. We mark these cases with an asterisk. The resulting best-fitting model provides an estimate of the T_{eff} of the host stars, which are summarized in Table 4. The results show that the T_{eff} of the parent stars are in the range of 4750-6500 K which corresponds to spectral types between K3 and F5. According to the T_{eff} found in the fit, we derive stellar radii and masses and calculate the surface gravity $\log g$ using 1-5 Gyr isochrones for solar metalicity obtained from the Dartmouth stellar evolution database (Dotter et al., 2008). These values are reported in Tables 4 and 10 as $R1_\star$, $M_\star$, and $\log g_1$. The error ranges of the stellar radii is determined by assuming a precision of 250 K which is the step size of the grid used in the VOSA fitting. Figure 9 shows an example of the VOSA fit of our best candidate 19b1-02162.

5.2. Secondary eclipse fit

For each candidate we tested the possibility that we actually detected an eclipsing binary system with similar eclipse depths where the primary and secondary eclipse have been folded together at half the binary period. In order to do this test, we fold the light curve of each candidate with double the detected period and fit a primary and secondary eclipse which are offset by 0.5 phase units assuming a circular orbit. Note that under this assumption, our candidate sample may be contaminated with eclipsing binaries in high eccentric orbits. However, Devor (2005) shows that only ~10% of the binaries studied there with periods shorter than 12 days have eccentricities higher

---

[4] http://svo2.cab.inta-csic.es/theory/vosa/
[5] http://ned.ipac.caltech.edu/forms/calculator.html

Table 3. List of new candidates around F-G-K stars detected in this work.

Object	Data-set	α	δ	u	g	r	i	z	Z	Y	J	H	K
19b1-02162	AP/DI	293.0112	36.4848	19.00	17.73	17.13	16.89	16.76	16.37	16.22	15.93	15.49	15.37
19f3-06991	AP	293.4682	36.4995	15.97	14.66	14.26	14.13	14.07	13.62	13.56	13.34	13.07	13.02
19b3-09004	DI	293.5208	36.8839	17.97	16.60	16.03	15.80	15.67	15.25	15.17	14.85	14.45	14.39
19g1-11212	AP	293.6753	36.1420	16.57	15.40	14.93	14.81	14.74	14.32	14.25	14.01	13.73	13.65
19c4-02952	DI	293.8666	36.7571	18.53	17.38	16.97	16.79	16.70	16.23	16.11	15.83	15.51	15.46
19h1-00325	AP	294.1531	36.0794	19.55	17.18	16.19	15.84	15.60	15.28	15.03	14.60	14.09	13.91
19b3-05398	AP	293.4401	36.7404	20.51	18.67	18.08	17.81	17.65	17.24	17.12	16.78	16.40	16.33
19e1-05755	DI	292.6870	36.2186	18.04	17.09	16.54	16.29	16.20	15.84	15.73	15.42	15.08	15.01
19b4-04138	AP	292.9365	36.7902	17.04	15.70	15.18	14.95	14.86	14.38	14.28	13.96	13.54	13.47
19b2-01819	DI	293.5220	36.4675	18.27	16.95	16.48	16.32	16.25	15.86	15.75	15.46	15.13	15.07

Notes. The second column shows the light curve data set in which the candidates have been detected. The coordinates (J2000.0) are listed in columns 3 and 4. The remaining columns provide broad band photometric measurements of our candidates in ten different filters. The u, g, r, i and z AB-magnitudes were obtained from the Sloan Digital Sky Survey (SDSS) and the Z, Y, J, H, K magnitudes are WFCAM measurements in the Vega-system.

Table 4. Characterization of host stars.

Object	T_{eff}(K)	Spectral Type	$\log g_1$	$\log g_2$	A_v	Distance(pc)	$R1_\star (R_\odot)$	$R2_\star (R_\odot)$	$M_\star (M_\odot)$
19b1-02162	5500	G8	4.56	4.32	0.21*	2188	$0.85^{+0.07}_{-0.05}$	$1.12^{+0.07}_{-0.12}$	$0.95^{+0.07}_{-0.06}$
19f3-06991	6500	F5	4.31	4.05	0.35	1127	$1.23^{+0.20}_{-0.10}$	$1.74^{+0.38}_{-0.16}$	$1.25^{+0.13}_{-0.08}$
19b3-09004	5750	G5	4.52	4.27	0.28	1472	$0.92^{+0.08}_{-0.07}$	$1.22^{+0.03}_{-0.04}$	$1.02^{+0.07}_{-0.07}$
19g1-11212	6250	F7	4.41	4.00	0.22*	1330	$1.13^{+0.20}_{-0.12}$	$1.78^{+0.27}_{-0.18}$	$1.17^{+0.09}_{-0.08}$
19c4-02952	6250	F7	4.41	4.01	0.44*	3119	$1.13^{+0.20}_{-0.12}$	$1.77^{+0.11}_{-0.07}$	$1.17^{+0.09}_{-0.08}$
19h1-00325	4750	K3	4.57	4.43	0.16	773	$0.71^{+0.03}_{-0.04}$	$0.89^{+0.08}_{-0.05}$	$0.78^{+0.04}_{-0.05}$
19b3-05398	6000	G0	4.47	4.19	0.45	4345	$1.00^{+0.13}_{-0.08}$	$1.39^{+0.08}_{-0.07}$	$1.09^{+0.17}_{-0.07}$
19e1-05755	6000	G0	4.47	4.12	0.38	2208	$1.00^{+0.13}_{-0.08}$	$1.51^{+0.06}_{-0.14}$	$1.09^{+0.17}_{-0.07}$
19b4-04138	5750	G5	4.52	3.96	0.45	506	$0.92^{+0.08}_{-0.07}$	$1.74^{+0.03}_{-0.05}$	$1.02^{+0.07}_{-0.07}$
19b2-01819	6250	F7	4.41	3.93	0.38	2559	$1.13^{+0.20}_{-0.12}$	$1.94^{+0.04}_{-0.05}$	$1.17^{+0.09}_{-0.08}$

Notes. The T_{eff} is derived from SED-fitting. We use 1-5 Gyr isochrones obtained from the Dartmouth stellar evolution database (Dotter et al., 2008) to estimate $R1_\star$, $\log g_1$ and $M_\star$. The extinction values (A_v) found in the SED fitting are reported in column 6. In the three cases marked with an asterisk the best fitting extinction is higher than the total extragalactic extinction and we report the extinction that corresponds to the minimum χ^2 within the allowed extinction range. The stellar radii $R2_\star$ correspond to the best fitting analytic transit model (see Section 5.3). The values of $\log g_2$ reported in column 5 are estimated from the stellar radii $R2_\star$, which tend to be higher than $R1_\star$, resulting in lower $\log g_2$. The distances reported in column 7 are estimated utilizing the extinction values found in the VOSA analysis, the i-band magnitudes reported in Table 3 and the absolute magnitudes M_i which are obtained from the isochrones.

than 0.1. Therefore, the possible contamination is low to start with. Moreover, any candidate with a clear deeper secondary eclipse would be rejected during our visual inspection. Both the primary and secondary eclipses are first fitted with a box and subsequently re-fitted with a symmetrical trapezoid as described in Section 4. A significant difference between the depths of the primary and secondary eclipse indicates that the candidate could be an eclipsing binary rather than a star with a planet. Also a comparison of the χ'^2_{dof} of the binary fit to the χ^2_{dof} of the fit with the planet period can indicate that the candidate is actually a binary with similar eclipse depths. We would like to point out that the decision of presenting either the planet or binary periods (Figures 16 and 17) included a visual examination of the folded light curves. This inspection showed that χ^2_{dof} and eclipse depths differences cannot be used blindly for the discrimination, since they closely depend on the number of points during the eclipses and box-fitting parameters. Note that the trapezium fit is only a crude model of a transit light curve and in some cases

we found that the depth estimated by our algorithm did not reflect the true depth as one sees in the folded light curves. In summary, the discrimination between both scenarios based on the χ^2_{dof} and eclipse depths values is only used as a hint to select either the planet or binary period rather than a decisive proof of the nature of the candidate. The final decision to classify our candidates was done case-by-case and primarily based on the best fitting radius as found in the analytic transit fit (see Section 5.3). Table 5 summarizes the results of the secondary eclipse fit analysis.

5.3. Transit fit

We carried out an improved fit to the J-band light curves of the candidates using analytic transit models proposed by Mandel & Agol (2002). For two candidates (19b1-02162 and 19b2-01819), we used additionally an i'-band light curve, covering one

**Table 5.** Comparison between the planet and binary scenario.

Object	V	$dp(\%)$	χ^2_{dof}	χ'^2_{dof}	$dp'_1(\%)$	$dp'_2(\%)$	V'_1	V'_2
19b1-02162	0.25	2.05	1.3792	1.3438	2.54	1.37	0.25	0.00
19f3-06991	0.56	0.81	1.0087	0.9545	1.08	0.47	0.58	0.33
19b3-09004	0.31	3.07	4.3247	4.2817	3.44	2.87	0.54	0.01
19g1-11212	0.37	1.49	1.4751	1.4301	2.29	1.34	0.45	0.81
19c4-02952	0.57	4.13	3.3622	3.3617	3.73	3.86	0.00	0.53
19h1-00325	0.43	3.11	4.0514	4.0172	2.92	3.05	0.16	0.38
19b3-05398	0.29	2.66	0.9802	0.9739	2.91	2.55	0.48	0.36
19e1-05755	0.29	1.76	1.7486	1.7211	2.54	1.66	0.80	0.54
19b4-04138	0.64	2.53	1.7270	1.7041	2.51	2.36	0.66	0.62
19b2-01819	0.45	2.80	2.7123	2.6819	2.74	3.07	0.61	0.65

Notes. Comparison of the eclipse shapes, eclipse depths and χ^2_{dof} values of the planet scenario (left side of the table) and binary scenario (right side of the table).

Table 6. Results from the transit fit.

Candidate	Period(days)	t_0	$i(°)$	$R_{planet}(R_{Jup})$	$R_{planet,min}(R_{Jup})$	$R_{planet,max}(R_{Jup})$	χ^2_{dof}	Classification
19b1-02162	0.59862739	2454317.7883529	72.01	1.61	1.40	1.97	1.31	P
19f3-06991	0.71482077	2454318.3894489	66.54	1.65	1.43	3.26	1.00	B
19b3-09004	3.55921358	2454320.9406801	84.31	2.22	2.10	2.32	2.07	B
19g1-11212	2.77301797	2454318.9644598	80.23	2.29	3.44	1.94	1.21	B
19c4-02952	3.42965118	2454319.6314035	82.25	3.54	3.36	3.81	1.84	B
19h1-00325	0.80767863	2454318.2698431	72.23	3.97	2.10	4.20	2.01	B
19b3-05398	0.73369311	2454317.9513207	67.12	4.20	3.53	4.99	1.18	B
19e1-05755	0.77250704	2454318.1282676	64.34	5.30	3.00	13.37	1.21	B
19b4-04138	1.10663897	2454318.0883407	67.34	6.14	4.17	8.32	1.30	B
19b2-01819	0.82989549	2454318.2785263	53.23	15.59	15.43	15.98	1.27	B

Notes. Orbital and planetary parameters derived from the analytic transit model fitting. Only one candidate, 19b-1-02162, is considered to be a planet candidate. All other candidates are too large and most likely transiting brown dwarfs or low-mass stars.
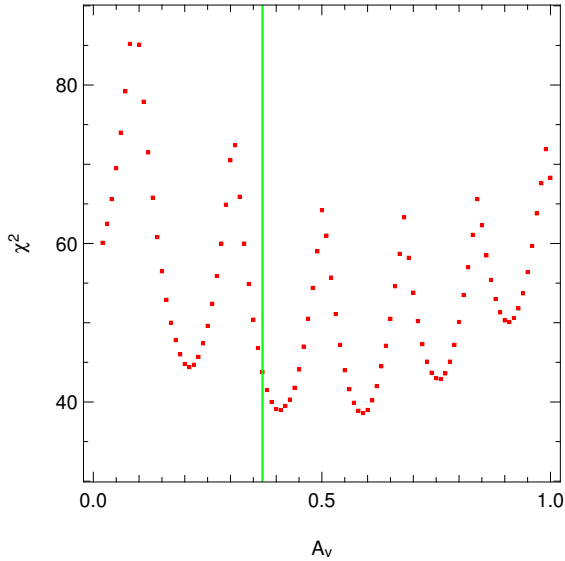

Fig. 8. χ^2 as a function of the input visual extinction value used in the SED fit of our planet candidate 19b1-02162. Although the value of $A_v \sim 0.6$ mag results in the lowest χ^2, we use the value of $A_v = 0.21$ mag based on the upper limit extinction adopted from the NASA/IPAC Extragalactic Database, since an extinction of $A_v = 0.6$ mag would be physically non-realistic. The upper limit mentioned above is pointed out with the green solid line. The periodic distribution of the χ^2 is due to the variation of six different stellar spectral-types.
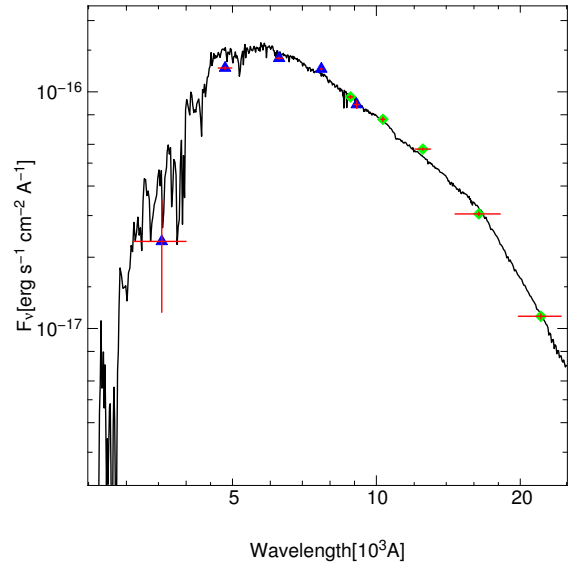

Fig. 9. Best Kurucz ATLAS9 model derived with VOSA (black line) for the SED of 19b1-02162 . The effective temperature of the best fitting model is $T_{eff} = 5500$ K for an extinction of $A_v = 0.21$. Blue triangles represent the SDSS photometry while the green diamonds correspond to the WFCAM photometry. Vertical and horizontal errors bars are the flux uncertainties and the equivalent width of each pass-band.

full eclipse, which was obtained in a photometric follow-up campaign at the Isaac Newton Telescope on La Palma. In these cases we performed a simultaneous fit to both light curves. The
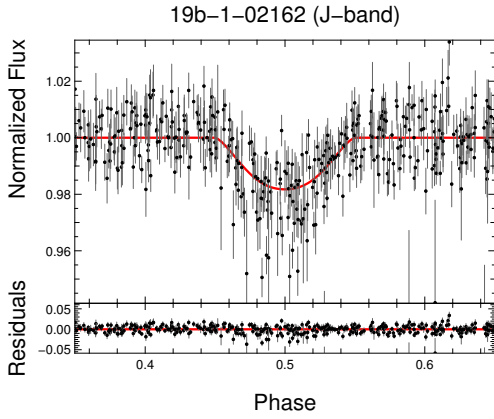
Fig. 10. Best fitting model of 19b-1-02162 using the J-band light curve. The top frame shows the best fit, whereas the bottom frame represents the residuals of the fit.
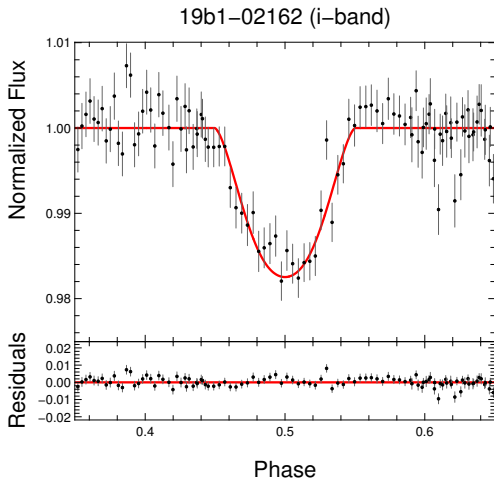
Fig. 11. Best fitting model of 19b-1-02162 using the i'-band light curve.

transit light curve model depends on quadratic limb-darkening coefficients, which were deduced as linear interpolations in T_{eff} and $\log g$ of the values listed in Claret & Bloemen (2011). We used the T_{eff} of host stars that were previously obtained by the SED analysis (see Section 5.1) and the corresponding $\log g$ values from the 1-5 Gyr isochrones, assuming a solar metalicity [Fe/H]=0.0 and a micro turbulence of 2 km/s. We utilized the values derived from ATLAS atmospheric models using the flux conservation method (FCM). Alternatively, the values can be derived using the least-squares method (LSM). However, a transit fit-test using the values from the two different models showed the same goodness of the fit for both methods, so we have chosen the FCM over the LSM model without any specific preference. Using the WTS J-band light curve, we fitted the mean stellar density $\rho_\star \sim M_\star / R_\star^3$ in solar units, the radius ratio $R_{planet} / R_\star$, the impact parameter β_{impact} in units of $R_\star$, the orbital period P and epoch of the central transit t_0. The iterative fitting process required starting values for a series of input parameters, such as period, epoch of transit, planet radius and parameter related to the stellar companion, such as mass and radius. The period, epoch of transit and planet radius were obtained directly from the results provided by our transit detection algorithm, while the stellar parameters ($R1_\star$ and $M_\star$) were estimated by using the previously fitted T_{eff} from the 1-5 Gyr model isochrones for solar metalicity (Dotter et al.,

2008). From the best fitting transit model, we were able to calculate the intrinsic physical parameters of the candidates and host stars, such as R_{planet} and $R2_\star$.

The fitting procedure also enabled us to derive an error estimation of the fitted parameters. The errors were calculated using a multi-dimensional grid in which we searched for extreme points with $\Delta\chi^2=1$. This method corresponds to a variation of each single parameter while minimizing over the others. The results of the transit fit are listed in Table 4 and 6. Figures 10 and 11 show the best fitting model of our best candidate 19b-1-02162 in the J and i'-bands respectively.

### 5.4. Discussion of the candidates

Table 6 provides a list of our candidates sorted according to their best fitting radius. All candidates except for the first two have very large best fitting radii, larger than all transiting planets published so far. We therfore conclude that they are systems with a transiting brown dwarf or a low-mass stellar companion. The first two candidates have best fitting radii of 1.61 R_{Jup} and 1.65 R_{Jup}, however, the secondary eclipse fitting results in a slightly better χ^2_{dof} for the binary scenario and the primary and secondary eclipse depths differ. Indeed, looking at the folded light curves (Figure 16) the second candidate, 19f3-06991, is a clear case where the fit with the binary period reveals two well sampled eclipses with different depths. The first candidate is not as clear. Although the binary period fit shows two different eclipses with depths of 2.5 and 1.4 %, the single eclipse observed in the i'-band coincides with the deeper eclipse but has a depth of 1.8 % (see Figure 11), which is more close to the shallower eclipse. We therefore conclude that for this candidate the correct period is unclear and we propose it as a target for high precision photometric follow-up. Figure 12 shows a J-band image of 19b1-02162.

In order to estimate the number of planets that we expect to find, we calculate the overall detection efficiency in our simulations, being ~1.7 % and ~2.4 % for DI and AP light curves respectively. Accounting for an average geometrical probability of 11.9 % to see transits (as derived from our Monte-Carlo simulations) and using an occurance rate for short period Jupiter-sized planets of 0.5 % (Gould et al., 2006; Howard et al., 2012) we estimate the number of planets that we expect to find in the whole sample of 102 428 light curves to be 1.0 (DI) and 1.5 (AP). This is in very good agreement with the two planets that have been detected in the WTS so far (Birkby et al., 2013a,b; Cappetta et al., 2012).

6. Candidates detected around M-stars

6.1. Selection criteria for M-stars:

We optimized the selection criteria for M-stars by injecting artificial transit signals into the DI and AP light curves of our WTS M-star sample. The sample has been selected using color cuts (see above). The simulated planet radius was always 1 R_{Jup} and we used a flat period distribution between 0.8 and 10 days. Using the criteria presented above we optimized the selection of M-dwarf planet candidates for the DI and AP light curves allowing up to 200 detections on the unmodified light curves. As for the F-, G- and K-stars, we require the detected period differs by 1% from the simulated period, allowing also half or double of this value.
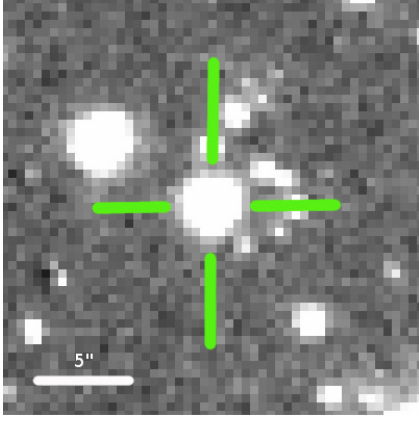
Fig. 12. Zoom-in showing the crowded neighborhood of the candidate 19b1-02162 on the sky. Our difference imaging pipeline is optimized to deal with such cases.

Tables 7 and 8 list the optimized criteria for the DI and AP light curves. Unlike in the case of F-, G- and K-stars, the fractional transit duration turned out to be a useful selection criterion. The V_{shape} parameter turned out not to be important since transits of Jupiter-sized planets orbiting M-dwarfs can be very V-shaped. Figure 14 shows the detection efficiency as a function of the apparent host star magnitude. Since the total number of M-stars is dominated by the faint end of the magnitude distribution the overall efficiency of the DI light curves is slightly higher with 44.8 % with respect to 43.8 % for AP light curves. Figure 13 shows the efficiency of the DI light curves as a function of the number of detections on the unmodified light curves. Our choice of 100 provides a high efficiency while still being managable to visually inspect.

Table 7. Optimized selection criteria for the DI M-star sample.

Criterion	Remaining objects	Removed objects	%
$J \leq 18$	10375	...	...
Removed alias period	7913	2462	23.73
S/N > 12	1450	6463	81.68
S/N-S/N$_{rem}$ > 5	536	914	63.03
Transit points > 8	164	372	69.40
V_{shape} < 1.00	164	0	0.00
Depth ≤ 30 %	138	26	15.85
Transit duration ≤ 0.06	98	40	28.98

Table 8. Optimized selection criteria for the AP M-star sample.

Criterion	Remaining objects	Removed objects	%
$J \leq 18$	10375	...	...
Removed alias period	8510	1865	17.98
S/N > 6	4411	4099	48.17
S/N-S/N$_{rem}$ > 2	278	4133	93.70
Transit points > 12	168	110	39.57
V_{shape} < 1.0	168	0	0.00
Depth ≤ 30 %	161	7	4.17
Transit duration ≤ 0.08	98	63	39.13

After visual examination of the 200 automatically selected candidates from the AP and DI light curves we identified 8 possible candidates. All of them were found both in the AP and DI
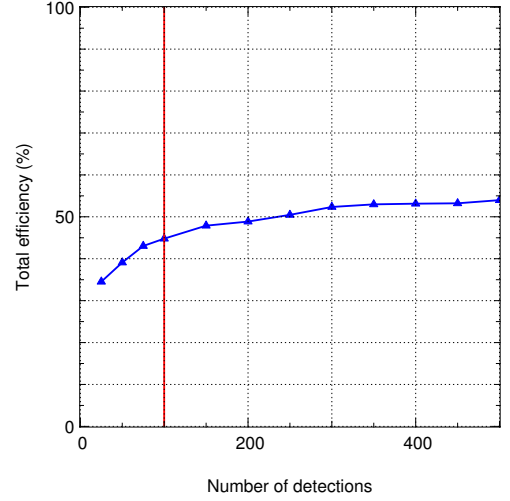
Fig. 13. Optimized total detection efficiency as a function of the number of detections on the unmodified DI light curves. The red line shows our limit of 100 detections.
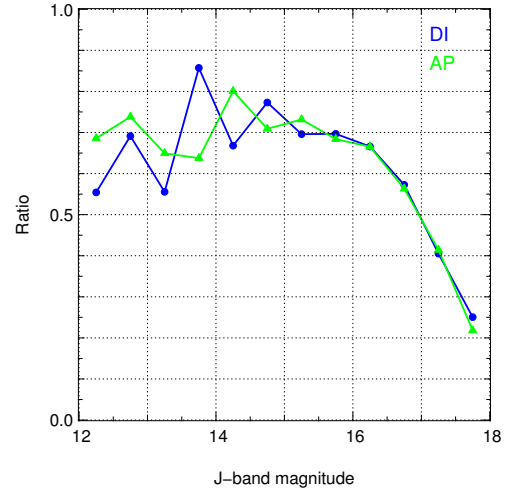
Fig. 14. Detection efficiency derived from the optimized selection parameters as a function of the host star magnitude.

light curves. Table 9 lists the coordinates and broad-band photometric data. As for the candidates found in the F-, G- and K-star sample we performed three different types of analyses to further asses the possibility of them being transiting planets. The result from the characterization of the host stars is shown in Table 10. For the M-dwarf analysis, we used the NextGen model atmospheres, which provides a wider range for low T_{eff}, being more appropriated for M-dwarfs. In this case, we restrict the limits to $T_{eff} = 1\,800\text{-}4\,500$K, [Fe/H]=0.0 and log g= 4.5-5.5. All 8 stars are in the range of $3300\,K \leq T_{eff} \leq 3900\,K$ corresponding to spectral types M5 to M0.

In the next step we performed a comparison of the planetary with a binary scenario corrsponding to a double-eclipse system at twice the detected period. The results are shown in Table 11, which reveal for two candidates, i.e. 19a1-02980 and 19a1-10878, different eclipse depths and a significantly better χ'^2.

Finally, we fit the J-band light curves of the 8 candidates with an analytic transit model (see Section 5.3). For all faint candidates with J≥17 mag we used the DI light curve since the photometric precision is higher compared to the AP light curves. For the brighter candidates 19a1-02980 and 19a1-10878 we used the

13

AP light curves. We determined the best fitting period, epoch of transit, orbital inclination and planet radius. The resulting values are listed in Table 12, where the smallest of our candidates has a radius of 2.53 R_{Jup}, which exceeds the radius of any planet previously reported. We show the folded light curves of our candidates around M-dwarfs in Figure 17.

Since none of our candidates has a best fitting radius in the planetary regime we conclude that they are all transiting brown dwarfs or low-mass stars and we therefore confirm the hypothesis presented in Kovács et al. (2013) about the null detection of Jupiter-sized planets around M-dwarfs in the WTS. Following their approach we derived a 95 % confidence upper limit on the giant planet occurrence rate for M-dwarfs. Kovács et al. (2013) analyzed all sources with J ≤ 17 mag and found an upper limit of 1.7-2.0 % for M0-M4 spectral types. In this work, we extended the search to all M-type stars with J ≤ 18 mag. The extra magnitude bin increased the number of sources by a factor of 2.8. In addition, we introduced an automatic selection procedure that reduces the number of candidates to be visually inspected to 100 for each set of light curves.

Assuming none of the candidates presented above are planets, we set an upper limit on the giant planet occurrence rate. Using equation (6) of Kovács et al. (2013) and the overall detection efficiency of 44.8 % for DI light curves, the average geometrical probability to see eclipses and the total number of sources of 10 375, the resulting upper limit is 1.1 %.

7. Other applications of the WTS DI light curves

In the previous sections we discussed the benefits of using the WTS DI light curves to detect transiting planet candidates, particularly when searching for objects with faint magnitudes (J > 16). The DI light curves can be used for additional analyses, such as detection and characterization of faint variable stars. In the next sections we describe two examples of the results presented by Nefs et al. (2012) and Birkby et al. (2012), which describe the discovery of extremely-short period M-dwarf eclipsing binaries and M-dwarf eclipsing binaries (MEBs) in the WTS. The motivation of showing these cases is to demonstrate that DI light curves are able to improve the results reported in the literature and provide new eclipsing binaries candidates when extending the search to fainter magnitudes.

7.1. Extremely-short period eclipsing binaries

Eclipsing binary stars with extremely-short periods below ∼ 0.22 days are very rare systems (Norton et al., 2011; Rucinski, 1992). So far, only a few of such objects have been discovered (e.g. Dimitrov & Kjurkchieva 2010; Maceroni & Montalbán 2004). The parameters of these systems can put strong constraints on formation and evolution theories of low-mass stars (Derekas et al., 2007; Devor, 2005). Recently, Nefs et al. (2012) reported a sample of 31 eclipsing binaries with periods smaller than 0.3 days found in the WTS 03, 07, 17 and 19h fields. Four of them are M-dwarf binaries with orbital periods considerably shorter than the sharp cut-off period of ∼ 0.22 days. We ran our detection algorithm on the DI light curves using the same input parameters reported in Nefs et al. (2012). We reproduce periods and t_0 values of the objects reported previously. In addition, we detected five new eclipsing binaries with periods shorter than 0.23 days. All systems satisfy the color cuts and fit with the red

sample (i.e M-dwarfs) presented in Nefs et al. (2012). We additionally use the SDSS color criteria from Ivezić et al. (2005) to eliminate the possibility of being in presence of RR Lyrae. Another cases of false-positives are caused by contamination effects from nearby stars and stellar variability originated by star spots. However, we reject both scenarios, since DI method is designed to reduce the effects produced by very near stellar neighbors and the phase folded light curves do not present a large scatter in their amplitude, which is generally an indication of variability generated by star spots. Table 13 lists the parameters of these systems. Note that for 19c-2-10801, the periodic signal could not be found in the AP light curve at all. We checked for a missmatch in the cross-identification procedure but could not find any object in the vicinity with a comparable variability. We show the folded light curves of all five objects in Figure 18.

In order to show the improvement in the precision of the DI light curves at faint magnitudes, we carry out a statistical comparison of the AP and DI light curves for the system 19e-3-11606, which has a brightness of J=17.97 mag. Figure 15 shows the phase-folded DI and AP light curves and the RMS with respect to the mean in 40 equally spaced bins. The horizontal lines show the 4σ clipped RMS for both light curves which are 0.050 and 0.062, respectively. The DI light curve therefore has an RMS that is about 12 mmag lower, being a little bit less than what we expected for a J=18.0 mag object. Looking at the other four detected objects we find that this is a general trend. The lower difference in RMS can be explained by the fact that we are looking at variable objects for which the *sysrem* algorithm cannot reduce systematic effects in an efficient way. It seems that the AP light curves are less affected by this than the DI light curves.

7.2. M-dwarf eclipsing binaries

Recently, Birkby et al. (2012) reported the detection of 16 M-dwarf eclipsing binary systems (MEBs) with J<16 mag found in the WTS AP light curves. These systems are particularly interesting because they provide important information about the fundamental properties of the most abundant stars in our Galaxy (Henry et al., 1997). Nevertheless, the existing theoretical models that describe the evolution of low-mass stars differ from the observed properties of M-dwarfs (López-Morales & Ribas, 2005). More observations and characterization of MEBs can provide new evidence to develop better and more accurate low-mass stellar evolution models (Birkby et al., 2012). We investigate the potential of extending the search for MEBs to fainter systems with magnitudes J ≤ 18 mag, making use of the improvement in the photometric precision of the DI light curves. In Table 12 we report eight candidates classified as eclipsing binary systems, where the objects 19a1-02980 & 19a1-10878 show strong evidence of being MEBs. The system 19a1-02980 was actually reported and confirmed as MEB in Birkby et al. (2012), which supports the remaining fainter detections, since they were identified through the same process. Furthermore, we found by an additional analysis carried out on the AP and DI light curves, a third system (19c4-06354) with similar characteristics as the two candidates mentioned above, so we also classify this object as MEB candidate. In Figure 17, we show the folded light curve of the 3 MEB candidates. The parameters associated with the main stellar companion of 19a1-02980 & 19a1-10878 are listed in Table 10. For the candidate 19c4-06354, we report a primary stellar companion with J-band = 17.97, in a short period system of $P \sim 0.76$ days and low T_{eff} of 3500 K. Due

Table 9. List of new candidates around M-dwarfs detected in this work.

Object	Data-set	α	δ	u	g	r	i	z	Z	Y	J	H	K
19b4-10711	AP/DI	293.0253	36.9168	24.10	21.85	20.35	19.07	18.51	17.99	17.63	17.17	16.53	16.25
19e3-01290	AP/DI	293.0688	36.5510	26.66	22.68	21.33	19.94	19.13	18.71	18.32	17.75	17.13	16.87
19a2-10046	AP/DI	293.2753	36.3017	26.61	23.24	21.08	20.19	19.34	18.96	18.57	17.97	17.35	17.16
19a1-02980	AP/DI	292.7127	36.3127	21.33	18.72	17.26	16.53	16.07	15.73	15.40	14.91	14.29	14.07
19a1-07499	AP/DI	292.5977	36.4613	26.39	21.57	19.97	18.98	18.46	18.08	17.68	17.16	16.54	16.30
19e3-05850	AP/DI	293.1396	36.6950	23.30	21.29	19.93	19.17	18.76	18.31	17.98	17.44	16.84	16.66
19a1-10878	AP/DI	292.5126	36.4273	22.94	20.63	19.14	18.10	17.48	17.20	16.82	16.29	15.67	15.40
19a1-01358	AP/DI	292.7526	36.4241	25.11	21.65	20.05	18.89	18.45	17.92	17.55	17.03	16.38	16.16

Notes. The second column shows the light curve data set in which the candidates have been detected. The coordinates (J2000.0) are listed in columns 3 and 4. The remaining columns provide broad band photometric measurements of our candidates in ten different filters. The u, g, r, i and z AB-magnitudes were obtained from the Sloan Digital Sky Survey (SDSS) and the Z, Y, J, H, K magnitudes are WFCAM measurements in the Vega-system.

Table 10. Characterization of host stars for the M-dwarfs sample.

Object	T_{eff}(K)	Spectral Type	$\log g_1$	$\log g_2$	A_v	Distance(pc)	$R1_\star(R_\odot)$	$R2_\star(R_\odot)$	$M_\star(M_\odot)$
19b4-10711	3400	M4	4.94	4.68	0.02	676	$0.33^{+0.07}_{-0.09}$	$0.44^{+0.01}_{-0.01}$	$0.34^{+0.09}_{-0.11}$
19e3-01290	3300	M5	5.02	4.49	0.18	703	$0.24^{+0.11}_{-0.09}$	$0.45^{+0.02}_{-0.02}$	$0.23^{+0.11}_{-0.10}$
19a2-10046	3500	M3	4.88	4.50	0.28*	1554	$0.40^{+0.05}_{-0.07}$	$0.61^{+0.02}_{-0.07}$	$0.43^{+0.05}_{-0.09}$
19a1-02980	3900	M0	4.70	4.21	0.15	522	$0.55^{+0.03}_{-0.03}$	$0.99^{+0.04}_{-0.05}$	$0.58^{+0.04}_{-0.02}$
19a1-07499	3600	M2	4.82	4.42	0.18	1063	$0.45^{+0.03}_{-0.05}$	$0.71^{+0.04}_{-0.06}$	$0.48^{+0.04}_{-0.05}$
19e3-05850	3800	M1	4.77	3.98	0.01	1572	$0.52^{+0.03}_{-0.04}$	$1.26^{+0.15}_{-0.02}$	$0.56^{+0.02}_{-0.04}$
19a1-10878	3600	M2	4.82	4.48	0.12	704	$0.45^{+0.03}_{-0.05}$	$0.66^{+0.01}_{-0.01}$	$0.48^{+0.04}_{-0.05}$
19a1-01358	3500	M3	4.88	4.89	0.11	844	$0.40^{+0.05}_{-0.07}$	$0.39^{+0.09}_{-0.03}$	$0.43^{+0.05}_{-0.09}$

Notes. The T_{eff} is derived from SED-fitting with VOSA. The stellar radii $R2_\star$ correspond to the best fitting analytic transit model (see Section 5.3). The distances reported in column 7 are estimated utilizing the extinction values found in the SED analysis, the i-band magnitudes reported in Table 3 and the absolute magnitudes M_i which are obtained from the isochrones.

Table 11. Comparison between the planet and binary scenario for candidates around M-dwarf.

Object	V	dp(%)	χ^2_{dof}	χ'^2_{dof}	dp$'_1$(%)	dp$'_2$(%)	V'_1	V'_2
19b4-10711	0.69	23.70	1.7020	1.6952	23.87	25.90	0.86	0.66
19e3-01290	0.66	24.98	1.0759	1.0715	25.52	19.95	0.71	0.52
19a2-10046	0.61	19.63	2.0426	2.0596	19.52	17.54	0.62	0.64
19a1-02980	0.72	2.17	1.7077	1.6537	2.70	1.42	0.71	0.79
19a1-07499	0.68	7.38	1.3803	1.3759	7.10	8.01	0.60	0.90
19e3-05850	0.00	7.85	1.1237	1.1203	7.48	7.42	0.00	0.16
19a1-10878	0.65	22.70	1.9194	1.7947	24.19	19.06	0.65	0.80
19a1-01358	0.91	4.67	1.3165	1.3142	5.28	3.30	0.66	0.21

Notes. Comparison of the eclipse shapes, eclipse depths and χ^2_{dof} values of the planet scenario (left side of the table) and binary scenario (right side of the table).

**Table 12. Characterization of canidates around M-dwarfs according the analytic transit fit.**

Candidate	Period(days)	t_0	$i(°)$	$R_{planet}(R_{Jup})$	$R_{planet,min}(R_{Jup})$	$R_{planet,max}(R_{Jup})$	χ^2_{dof}	Classification
19b4-10711	1.55274390	2454318.1664350	85.16	2.53	2.34	2.84	1.28	B
19e3-01290	2.46752082	2454318.6477813	85.86	2.64	2.34	3.20	1.01	B
19a2-10046	1.45677364	2454318.7173035	84.48	2.78	2.46	5.31	1.43	B
19a1-02980	1.05176697	2454318.6516446	72.80	3.25	1.93	6.95	1.31	B
19a1-07499	1.96038974	2454318.5897989	81.29	3.45	2.14	7.28	1.18	B
19e3-05850	9.20198442	2454320.1712614	86.81	3.48	3.30	5.03	1.06	B
19a1-10878	1.55498531	2454317.9578553	83.43	3.71	3.49	3.99	1.32	B
19a1-01358	1.10712079	2454318.6005745	76.76	4.94	1.71	7.12	1.09	B

Notes. Orbital and planetary parameters derived from the analytic transit model fitting. All candidates are too large and are most likely transiting brown dwarfs or low-mass stars.

Table 13. List of extremely short period eclipsing binary systems found in this work.

Object	α	δ	Period(days)	t_0	dp'_2/dp'_1	J	u	g	r	i	z	(r-i)	(i-z)	RMS(AP)	RMS(DI)
19c3-12753	294.3839	36.9062	0.1859752355	2454317.8449795	1.56	17.87	24.93	22.80	21.09	20.08	19.17	1.01	0.91	0.041	0.028
19b2-04235	293.3342	36.4255	0.1974392134	2454317.9485581	1.52	17.32	22.68	22.07	20.16	19.43	18.77	0.74	0.66	0.027	0.023
19c2-10801	294.2404	36.3471	0.1977343597	2454317.9436689	0.88	17.78	25.86	21.37	20.24	19.66	19.36	0.59	0.29	…	0.049
19c3-11606	293.2310	36.6396	0.2106563732	2454317.7894282	1.45	17.97	25.01	21.71	20.31	19.67	19.40	0.65	0.26	0.062	0.050
19c1-00478	293.8732	36.4661	0.2261831592	2454317.8755733	1.57	17.18	23.53	20.44	19.40	18.70	18.35	0.69	0.36	0.028	0.022

Notes. Extremely short period eclipsing binary systems with period below 0.23 days. We list the period, epoch and eclipse depth ratio as well as the WFCAM J-band and SDSS ugriz photometry for each candidate. The last two columns provide information on the 4σ clipped RMS of the light curves after removing the periodic signal. In general the precision of the DI light curves is significantly better than the precision of the AP light curves. This is due to the fact that all objects are fainter than 17 mag in the J-band, which is in the regime where DI light curves present an improvement over AP light curves (see Section 3).
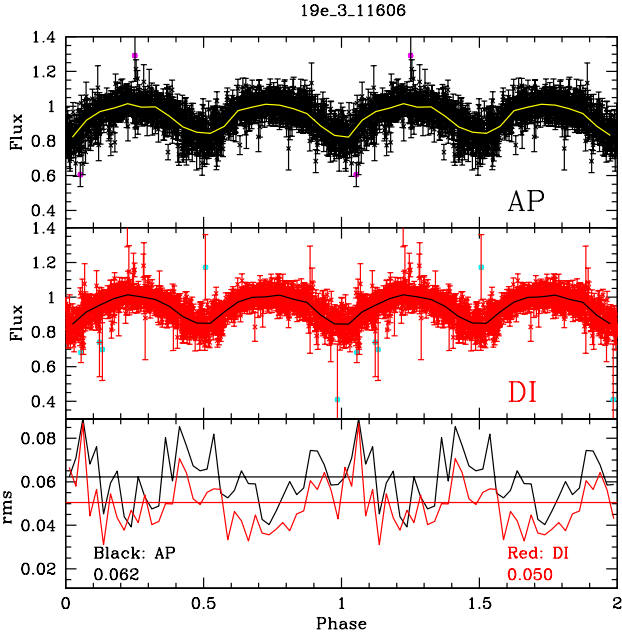
Fig. 15. Comparison between the AP and DI light curve of an extremely-short period eclipsing binary system (19e-3-11606) found with the DI light curves. Black and red points in the uppert two panels correspond to the AP and DI light curves respectively. The yellow and black solid lines connect the median values in 40 bins with a size of 0.025 phase units. The lower panel shows the 4σ clipped RMS of the residuals in each bin after subtracting the median. The horizontal lines represent the average RMS of the residuals which are 0.062 and 0.050 for the AP and DI light curve respectively.

to the faint magnitude of the primary stellar companion, this MEB candidate was found only in the DI light curves. A more extensive and meticulous search for MEB systems in the DI light curves (which is out of the scope of this work) could potentially reveal many more detections in the future.

8. Conclusions

We carried out a quantitative comparison between the photometric precision of two different sets of light curves from the 19h field, which represents the most complete field of the WTS. The light curves were obtained using two different photometric techniques, AP and DI. The *sysrem* algorithm was used to re-

move systematic effects in both data sets and corrected the light curves by scaling the error bars. The WTS AP light curves reach a slightly better photometric precision (by ~1 mmag) than the DI light curves for objects brighter than J ≈ 15.5 mag. On the other hand, the DI light curves show a significant improvement of ~2-20 mmag for sources with magnitudes larger than J = 16 mag.

A modified version of the box-fitting algorithm was employed to search for transiting planets in the survey. Our algorithm uses the standard BLS to searches for the best trial period and subsequently makes a trapezoid re-fitting to the folded light curve, providing a new estimation of the transit depth. A χ^2 comparison shows that the new trapezoid fit provides better results than the traditional box-fitting. The algorithm also calculates a new parameter based on the geometry of the new trapezoid fit, the V-shape parameter. This parameter has proven to be very efficient in the identification and removal of eclipsing binaries from the candidate sample.

In order to select our candidates, we proposed a set of selection criteria, 6 of them are based on the experience of previous works. Additionally, 2 new criteria were incorporated, which take advantage of the results obtained with our transit detection algorithm, such as the V-shape parameter. The set of parameters of our selection criteria was optimized using Monte Carlo simulations by injecting transit signals to both the AP and DI light curves. The light curves were split in two different sets, one for F-G-K-stars, and a second for M-dwarfs. The optimization of the criteria was performed in both sets separately. The selection criteria have shown the capability of detecting 200 candidates in the DI and AP light curves from a original sample of ~ 475 000 F-G-K-stars, while 196 candidates were detected in both sets of light curves from the M-dwarfs sample. We carried out a visual examination on the detections and identified 18 relevant transit planet candidates.

In order to discriminate planetary from binary candidates, a detailed analysis of the 18 candidates was conducted, which provides physical parameters of the candidates and their host stars. The analysis includes a characterization of the parent star and a transit fit of the light curve using a realistic model proposed by Mandel & Agol (2002). Furthermore, we performed a secondary eclipse fit to the phase folded light curve using the double period to detect potential differences in the χ^2_{dof} and/or the depths of the primary and secondary eclipses that could be an indication of an eclipsing binary system. In our analysis, only one object is classified as a planet candidate, which is proposed for photometric follow-up. The remaining 17 candidates have large best fitting radii and are therefore classified as binary candidates.

No planet candidates orbiting an M-dwarf was found, therefore, the null detection presented in Kovács et al. (2013) was confirmed. A detailed sensitivity analysis allowed us to derive an upper limit on the occurrence rate of giant planets around M-dwarfs with periods below 10 days. Increasing the number of target stars by going one magnitude deeper, we were able to set a 95 % confidence upper limit of 1.1 %, which is significantly lower than any limit published so far. Another applications of the WTS DI light curves were reported. We presented the detection of five new ultra-short period eclipsing binaries with periods below 0.23 days and J > 17 mag. In addition, three detached M-dwarf eclipsing binary candidates were reported; two of them were found in both the AP and DI light curves, while the third and faintest candidate was only detected in the DI light curves sample. These results show that the DI light curves are able to reproduce and improve results reported in the literature. In conclusion, the WTS DI light curves are useful for many purposes, such as detection of transit planet candidates and rare eclipsing binary systems, especially when pushing the limits to fainter magnitudes.
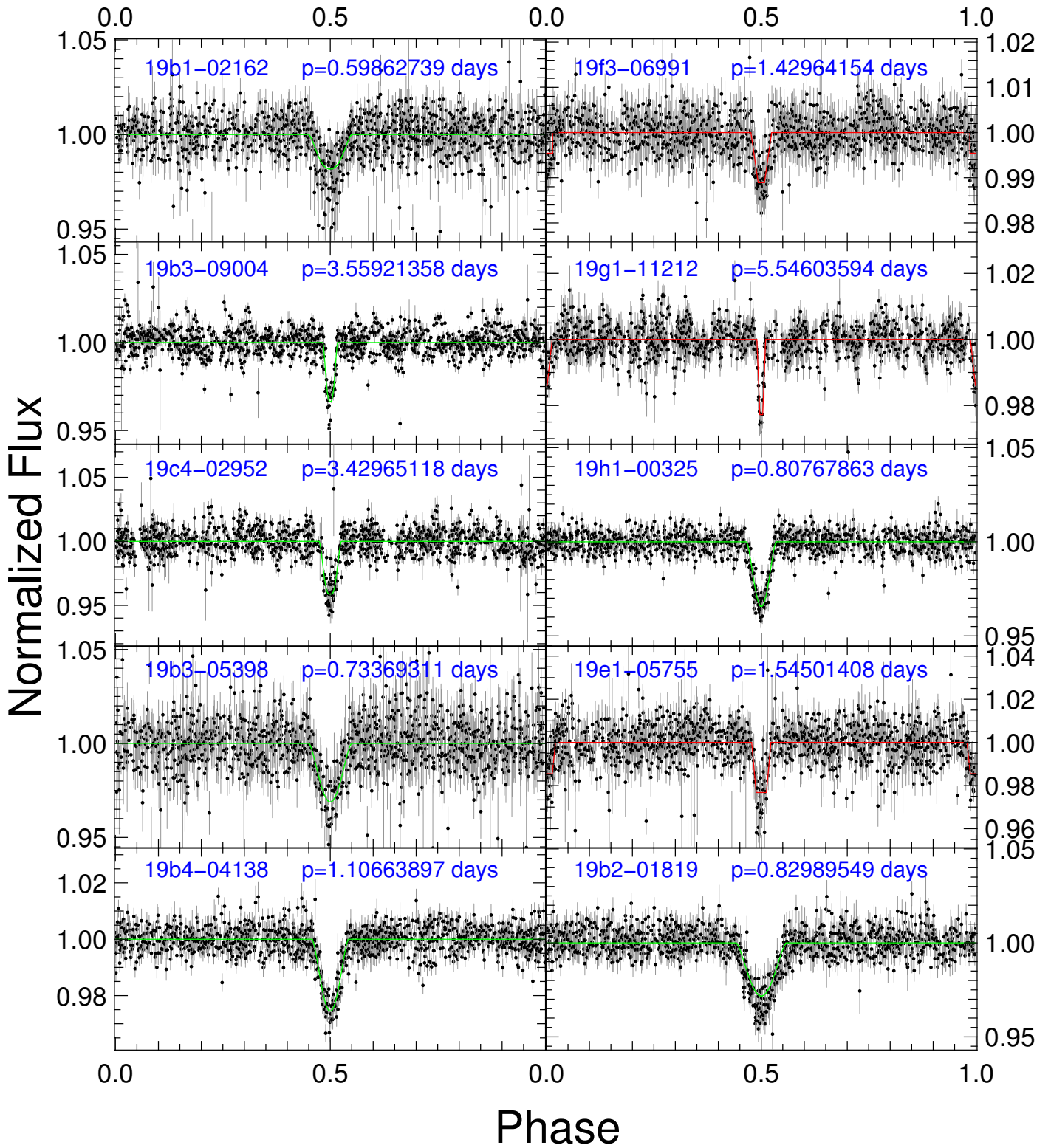
Fig. 16. Phase-folded light curves of the 10 candidates orbiting F-G-K stars found in the WTS 19h field. We overplot the best fitting single eclipse transit models (green lines) for all objects for which the binary scenario fit does not show an improvement over the single eclipse scenario. The light curves with two eclipses are shown together with the best fitting trapeziod model (red lines)
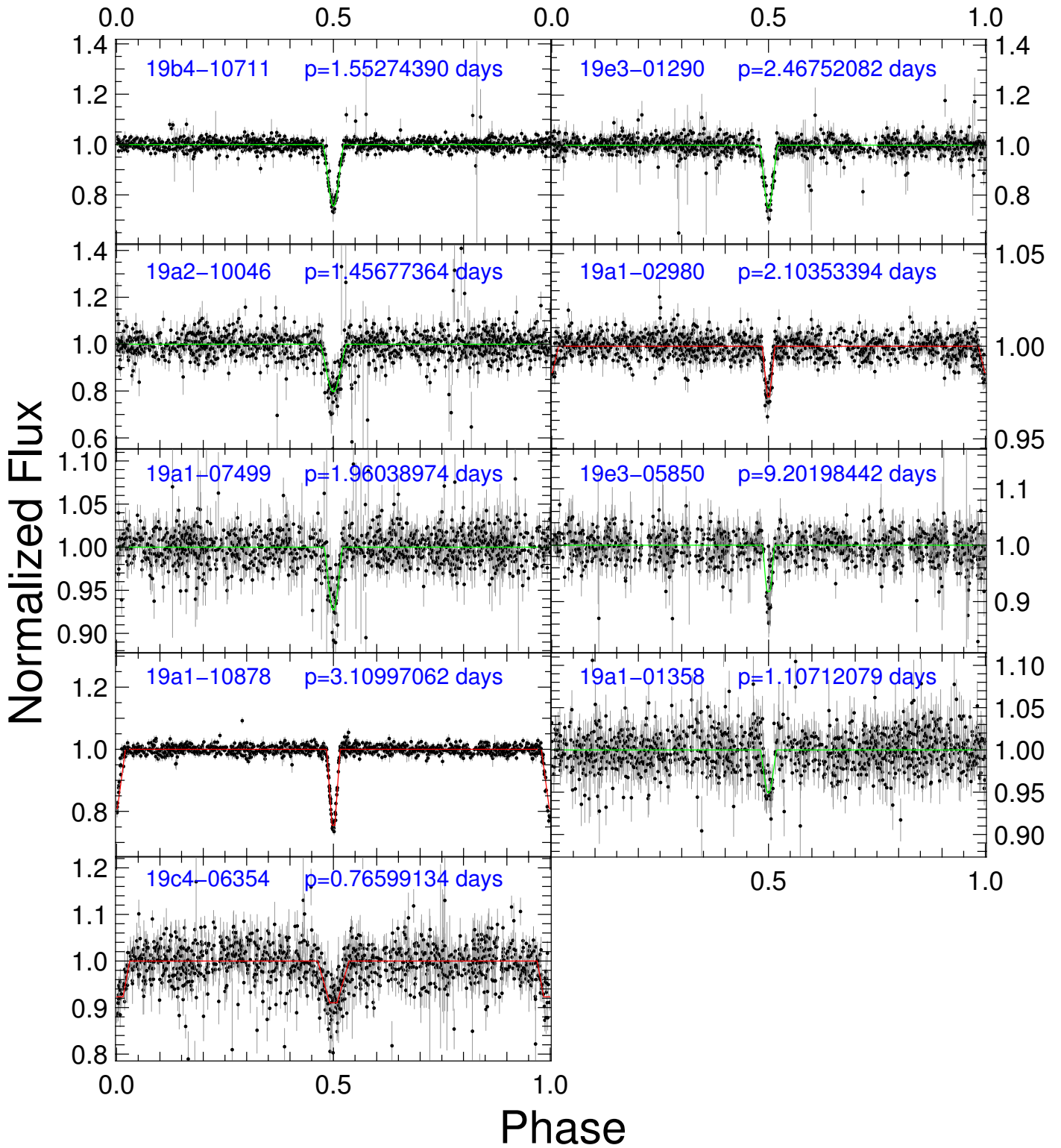
Fig. 17. Phase-folded light curves of the 8 candidates orbiting M-dwarfs found in the WTS 19h field. As it was done for the candidates around F-G-K-stars, we overplot the best fitting single eclipse with green-solid lines, whereas the light curves with two eclipses are shown together with the best fitting trapeziod model in red-solid lines. The objects with two eclipses are reported in Section 7.2 as MEB candidates. The objects 19a1-02980 and 19a1-10878 were found by our selection criteria during the process of transiting planet detection, whereas the system 19c4-06354 was separately detected by an additional analysis carried out on the AP and DI light curves.
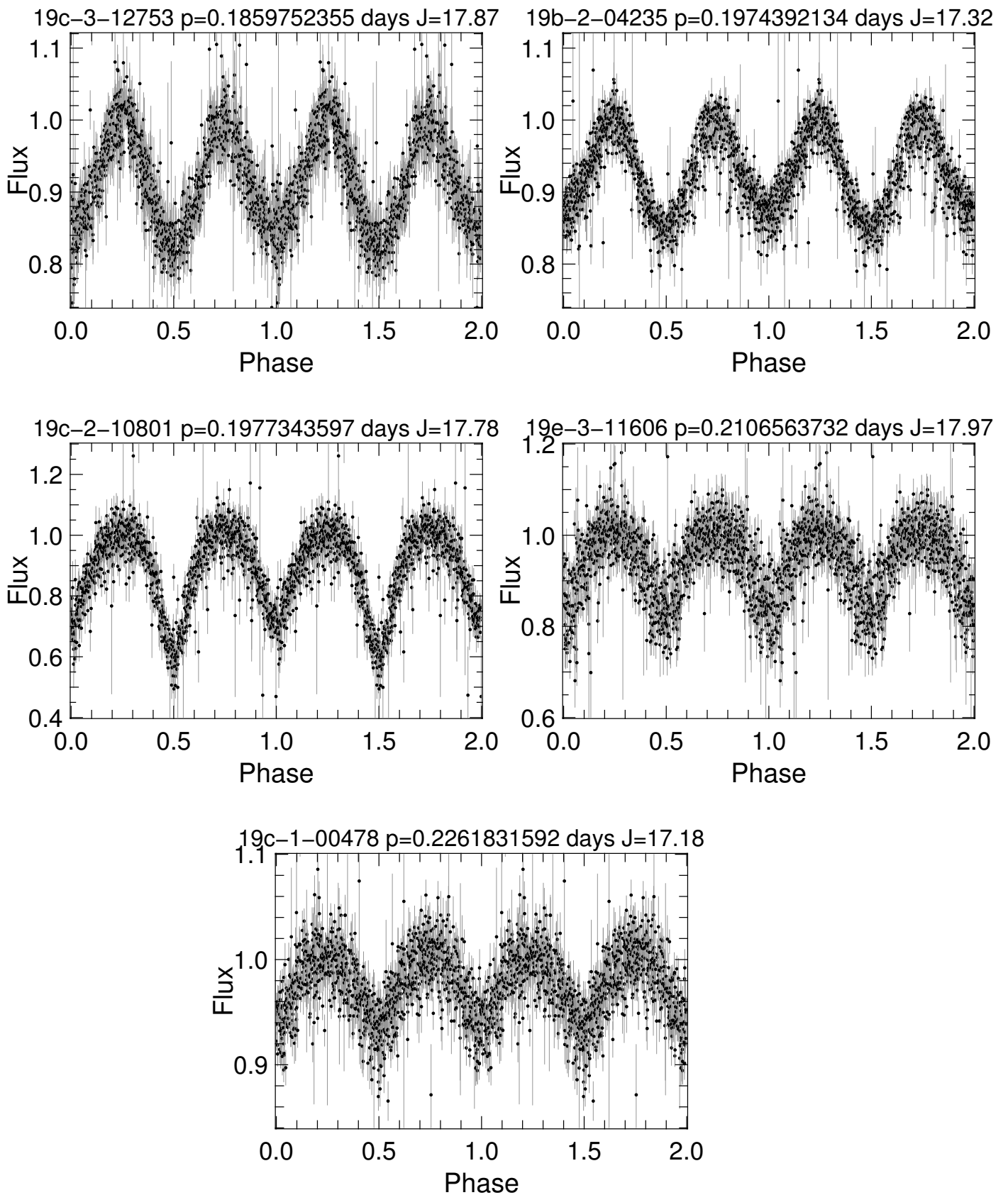
Fig. 18. Phase-folded light curves of the five extremely-short period eclipsing binaries found in this work.

References

Adelman-McCarthy, J. K. & et al. 2009, VizieR Online Data Catalog, 2294, 0

Aigrain, S., Barge, P., Deleuil, M., et al. 2008, in Astronomical Society of the Pacific Conference Series, Vol. 384, 14th Cambridge Workshop on Cool Stars, Stellar Systems, and the Sun, ed. G. van Belle, 270

Alard, C. & Lupton, R. H. 1998, ApJ, 503, 325

Baraffe, I., Chabrier, G., Allard, F., & Hauschildt, P. H. 1998, A&A, 337, 403

Barge, P., Baglin, A., Auvergne, M., & CoRoT Team. 2008, in IAU Symposium, Vol. 249, IAU Symposium, ed. Y.-S. Sun, S. Ferraz-Mello, & J.-L. Zhou, 3–16

Bayo, A., Rodrigo, C., Barrado Y Navascués, D., et al. 2008, A&A, 492, 277

Berta, Z. K., Irwin, J., Charbonneau, D., Burke, C. J., & Falco, E. E. 2012, AJ, 144, 145

Birkby, J., Nefs, B., Hodgkin, S., et al. 2012, MNRAS, 426, 1507

Birkby, J. L., Cappetta, M., Cruz, P., et al. 2013a, in European Physical Journal Web of Conferences, Vol. 47, European Physical Journal Web of Conferences, 1004

Birkby, J. L., Cappetta, M., Cruz, P., et al. 2013b, MNRAS, submitted

Borucki, W. J., Koch, D., Basri, G., et al. 2010, Science, 327, 977

Burke, C. J., Gaudi, B. S., DePoy, D. L., & Pogge, R. W. 2006, AJ, 132, 210

Cappetta, M., Saglia, R. P., Birkby, J. L., et al. 2012, MNRAS, 427, 1877

Castelli, F., Gratton, R. G., & Kurucz, R. L. 1997, A&A, 318, 841

Charbonneau, D., Brown, T. M., Latham, D. W., & Mayor, M. 2000, ApJ, 529, L45

Claret, A. & Bloemen, S. 2011, A&A, 529, A75

Defaÿ, C., Deleuil, M., & Barge, P. 2001, A&A, 365, 330

Derekas, A., Kiss, L. L., & Bedding, T. R. 2007, ApJ, 663, 249

Devor, J. 2005, ApJ, 628, 411

Dimitrov, D. P. & Kjurkchieva, D. P. 2010, MNRAS, 406, 2559

Dotter, A., Chaboyer, B., Jevremović, D., et al. 2008, ApJS, 178, 89

Giacobbe, P., Damasso, M., Sozzetti, A., et al. 2012, MNRAS, 424, 3101

Gould, A., Dorsher, S., Gaudi, B. S., & Udalski, A. 2006, Acta Astron., 56, 1

Hartman, J. D., Gaudi, B. S., Holman, M. J., et al. 2009, ApJ, 695, 336

Henry, G. W., Marcy, G. W., Butler, R. P., & Vogt, S. S. 2000, ApJ, 529, L41

Henry, T. J., Ianna, P. A., Kirkpatrick, J. D., & Jahreiss, H. 1997, AJ, 114, 388

Hodgkin, S. T., Irwin, M. J., Hewett, P. C., & Warren, S. J. 2009, MNRAS, 394, 675

Howard, A. W., Marcy, G. W., Bryson, S. T., et al. 2012, ApJS, 201, 15

Irwin, J., Charbonneau, D., Nutzman, P., & Falco, E. 2009, in American Institute of Physics Conference Series, Vol. 1094, 15th Cambridge Workshop on Cool Stars, Stellar Systems, and the Sun, ed. E. Stempels, 445–448

Irwin, J., Irwin, M., Aigrain, S., et al. 2007, MNRAS, 375, 1449

Irwin, M. & Lewis, J. 2001, New A Rev., 45, 105

Irwin, M. J. 1985, MNRAS, 214, 575

Ivezić, Ž., Vivas, A. K., Lupton, R. H., & Zinn, R. 2005, AJ, 129, 1096

Jehin, E., Gillon, M., Queloz, D., et al. 2011, The Messenger, 145, 2

Jenkins, J. M., Chandrasekaran, H., McCauliff, S. D., et al. 2010, in Society of Photo-Optical Instrumentation Engineers (SPIE) Conference Series, Vol. 7740, Society of Photo-Optical Instrumentation Engineers (SPIE) Conference Series

Kaltenegger, L. & Traub, W. A. 2009, ApJ, 698, 519

Kasting, J. F., Whitmire, D. P., & Reynolds, R. T. 1993, Icarus, 101, 108

Kleinmann, S. G., Lysaght, M. G., Pughe, W. L., et al. 1994, Ap&SS, 217, 11

Koppenhoefer, J., Afonso, C., Saglia, R. P., & Henning, T. 2009, A&A, 494, 707

Kovács, G., Hodgkin, S., Sipőcz, B., et al. 2013, MNRAS

Kovács, G., Zucker, S., & Mazeh, T. 2002, A&A, 391, 369

Law, N. M., Kraus, A. L., Street, R., et al. 2012, ApJ, 757, 133

López-Morales, M. & Ribas, I. 2005, ApJ, 631, 1120

Maceroni, C. & Montalbán, J. 2004, A&A, 426, 577

Mandel, K. & Agol, E. 2002, ApJ, 580, L171

Mayor, M. & Queloz, D. 1995, Nature, 378, 355

Mazeh, T., Guterman, P., Aigrain, S., et al. 2009, A&A, 506, 431

Meeus, J. 1982, Astronomical formulae for calculators, 43

Montalto, M., Piotto, G., Desidera, S., et al. 2007, A&A, 470, 1137

Nefs, S. V., Birkby, J. L., Snellen, I. A. G., et al. 2012, MNRAS, 425, 950

Norton, A. J., Payne, S. G., Evans, T., et al. 2011, A&A, 528, A90

Pietrukowicz, P., Minniti, D., Díaz, R. F., et al. 2010, A&A, 509, A4

Pont, F., Zucker, S., & Queloz, D. 2006, MNRAS, 373, 231

Robin, A. C., Reylé, C., Derrière, S., & Picaud, S. 2003, A&A, 409, 523

Rucinski, S. M. 1992, AJ, 103, 960

Scalo, J., Kaltenegger, L., Segura, A. G., et al. 2007, Astrobiology, 7, 85

Snellen, I. A. G., van der Burg, R. F. J., de Hoon, M. D. J., & Vuijsje, F. N. 2007, A&A, 476, 1357

Tamuz, O., Mazeh, T., & Zucker, S. 2005, MNRAS, 356, 1466

Tarter, J. C., Backus, P. R., Mancinelli, R. L., et al. 2007, Astrobiology, 7, 30

Tomaney, A. B. & Crotts, A. P. S. 1996, AJ, 112, 2872